Compositional editing of extracellular matrices by CRISPR/Cas9 engineering of human mesenchymal stem cell lines

Sujeethkumar Prithiviraj [1,2,3], Alejandro Garcia Garcia [1,2,3], Karin Linderfalk [1,2,3], Bai Yiguang [4], Sonia Ferveur [1,2,3], Ludvig Nilsén Falck [5], Agatheeswaran Subramaniam [5], Sofie Mohlin [6], David Hidalgo [1, 2,3], Steven J Dupard[1, 2,3], Deepak Bushan Raina [7], Paul E Bourgine [1,2,3].

[1]Cell, Tissue & Organ engineering laboratory, BMC B11, 22184, Department of Clinical Sciences, Lund Stem Cell Centre, Lund University, Lund, Sweden

[2]Wallenberg Centre for Molecular Medicine, Lund University, Lund, Sweden

[3]Lund University Cancer Centre, Lund University, Lund, Sweden

[4]Department of Orthopaedics, Nanchong central hospital, The second clinical Institute of North Sichuan Medical college Nanchong, Sichuan, China

[5]Division of Molecular Medicine and Gene Therapy, Lund Stem Cell Centre, Lund University, 22184 Lund, Sweden

[6]Division of Pediatrics, Clinical Sciences, Translational Cancer Research, Lund University Cancer Center at Medicon Village, Lund, 22363, Sweden

[7]The Faculty of Medicine, Department of Clinical Sciences Lund, Orthopedics, Lund 221 84, Sweden

Abstract

Tissue engineering strategies predominantly rely on the production of living substitutes, whereby implanted cells actively participate in the regenerative process. Beyond cost and delayed graft availability, the patient-specific performance of engineered tissues poses serious concerns on their clinical translation ability. A more exciting paradigm consist in exploiting cell-laid, engineered extracellular matrices (eECM), which can be used as off-the-shelf materials. Here, the regenerative capacity solely relies on the preservation of the eECM structure and embedded signals to instruct an endogenous repair. We recently described the possibility to exploit custom human stem cell lines for eECM manufacturing. In addition to the conferred standardization, the availability of such cell lines opened avenues for the design of tailored eECMs by applying dedicated genetic tools. In this study, we demonstrated the exploitation of CRISPR/Cas9 as a high precision system for editing the composition and function of eECMs. Human mesenchymal stromal/stem cell (hMSC) lines were modified to knockout VEGF and RUNX2 and assessed for their capacity to generate osteoinductive cartilage matrices. We report the successful editing of

32 hMSCs, subsequently leading to targeted VEGF and RUNX2-knockout cartilage eECMs. Despite the
33 absence of VEGF, eECMs retained full capacity to instruct ectopic endochondral ossification. Conversely,
34 RUNX2-edited eECMs exhibited impaired hypertrophy, reduced ectopic ossification and superior cartilage
35 repair in a rat osteochondral defect. In summary, our approach can be harnessed to identify the necessary
36 eECM factors driving endogenous repair. Our work paves the road towards the compositional eECMs
37 editing and their exploitation in broad regenerative contexts.

38

39 **Introduction**

40 Extracellular matrices (ECMs) are complex networks of proteins providing tissue structural and mechanical
41 support, but also acting as growth factor storing and presenting entities[1]. As such, ECMs are receiving
42 increasing attention in tissue engineering as templates capable of guiding homeostasis, remodeling, and
43 regenerative processes[2,3,4].
44 ECMs can be derived from native tissue or organs (native ECMs, nECMs) by applying a decellularization
45 step which effectively removes the cellular fraction. The resulting nECMs are commonly used as
46 biomaterials in regenerative medicine[5,6], offering a natural biocompatible structure. However, they suffer
47 from substantial batch-to-batch variation with their properties being largely affected by the tissue source
48 and the decellularization process[5,7]. Importantly, while displaying a high level of biological complexity and
49 fidelity, the composition of nECMs cannot be tailored to specific needs.
50 A valuable option emerged from recent advances in bioengineering which led to the development of
51 synthetic ECMs (sECMs). These tunable materials are predominantly composed of biopolymers such as
52 poly (lactic acid) (PLA), poly (glycolic acid) (PGA), poly (lactic co-glycolic acid) (PLGA) and Poly (ethylene
53 glycol) (PEG), which can be functionalized with bioactive substances such as peptides, growth factors or
54 enzymes[8,9,10,]. The possible modulation of sECM's composition and chemistry offers precise control over
55 their mechanical properties, degradability, and temporal release of instructive molecules towards
56 improved tissue repair. Despite holding great promises, yet their structure and function remain simplified
57 compared to their native counterpart [11,12].
58 With the aim of combining high biological fidelity and design flexibility, engineered ECMs (eECMs) have
59 become a credible alternative. Those result from the exploitation of stem/progenitor populations capable
60 of depositing ECMs under specific in vitro culture conditions[13,14,15,16], which can be subsequently isolated
61 from the cellular fraction and exploited as a cell-laid product. Early studies were conducted using eECM
62 derived from primary cells, exhibiting variable performance associated with the inter-donor variability[17,18].

63 Most recently, we demonstrated the possibility to standardize the production of eECMs through the
64 engineering of dedicated human mesenchymal stromal/stem cell (hMSC) lines[19]. Precisely, the
65 Mesenchymal Sword of Damocles – BMP2 (MSOD-B) line offered the generation of eECMs in the form of
66 human cartilage templates[20]. Those cartilage templates can be further devitalized, lyophilized, and stored
67 as an *off-the-shelf* tissue, retaining remarkable bone formation capacity by instructing endochondral
68 ossification[21,22].
69 The exploitation of cell lines as an unlimited cell source for eECM generation offers unprecedented
70 standardization in graft production and performance. Meanwhile, it also consists of a robust cellular
71 platform facilitating their further genetic engineering, to achieve the production of eECMs tailored in
72 composition and function. Towards this objective, CRISPR/Cas9 appears as a versatile and efficient gene-
73 editing tool. While this technology has been extensively used for genetic screening or disease
74 modeling[23,24,25], the possibility to edit hMSCs and study the compositional impact on deposited eECMs has
75 not been investigated so far.
76 In this study, we aim at demonstrating that CRISPR/Cas9 can be applied as an editing tool for the
77 engineering of custom eECMs. As proof-of-principle, our strategy relies on the CRISPR/Cas9-guided editing
78 of the MSOD-B line for knocking out Vascular endothelial growth factor (VEGF) and Runt related
79 transcription factor 2 (RUNX2), respectively a key pro-angiogenic protein and transcription factor critically
80 involved in the endochondral ossification pathway. The resulting hMSC lines will be evaluated for their
81 capacity to generate hypertrophic cartilage in vitro and instruct tailored skeletal tissue formation in vivo
82 as cell-free and lyophilized templates. If successful, our study is expected to validate the use of
83 CRISPR/Cas9 for eECMs edited in composition, while providing a novel platform towards decoding the
84 necessary molecular signals driving effective tissue repair.
85

86 **Results**

87 **CRISPR/Cas9 editing of hMSC lines lead to efficient VEGF knockout in cartilage tissues.**

88 VEGF is a known master regulator of angiogenesis[26] and a key mediator of endochondral ossification.
89 When reaching hypertrophy, chondrocytes highly express VEGF, prompting vasculature invasion and
90 subsequent osteoprogenitor recruitment. This was proven to be essential for cartilage template
91 remodeling into bone and bone marrow[27]. Here, we thus first aimed at engineering a hMSC line
92 CRISPR/Cas9-edited for VEGF knockout and evaluate the corresponding impact on cartilage and
93 endochondral bone formation (Figure 1A). To this end, specific guide RNAs (gRNAs) targeting different

94 regions of the VEGF gene but conserved across all isoforms of VEGF were designed based on a previously
95 established protocol[28]. Three gRNAs targeting exon 1 (VEGF_1.1, VEGF_1,2, VEGF1.3), one targeting exon
96 2 (VEGF_2.1), and one targeting exon 8 (VEGF_8.1) were designed (Figure 1B, Supplementary Figure 1A).
97 These gRNAs were cloned into the pU6-(BbsI)_CBh-Cas9-T2A-mCherry vector encoding the Streptococcus
98 pyogenes Cas9 (SpCas9) machinery. Following transfection in MSOD-B cells, single cell clones were sorted
99 based on the transient mCherry expression and expanded for characterization (Figure 1A). Out of 163
100 single clones, 14 could be successfully expanded (8.5 %). From these clones, five were retrieved from the
101 gRNA 1.1, six from gRNA 1.3 and three from gRNA 8.1. In order to assess a successful editing and directly
102 correlate it to a knockout of VEGF, an ELISA assay was performed to measure the concentration of VEGF
103 in the supernatant of expanded MSOD-B clones (Figure 1C). In non-edited cells (MSOD-B, control), 5000
104 pg/mL were secreted and detected by ELISA. From the successfully expanded clones, most of them
105 showed reduced but non-abolished secretion of VEGF. However, two clones exhibited undetectable levels
106 of VEGF, both resulting from the gRNA targeting the Exon1 of the VEGF gene. These clones were defined
107 as MSOD-BΔV1 and MSOD-BΔV2 and further characterized for their capacity to form cartilage.

108 To this end, clones were expanded and seeded on collagen scaffold and induced for three weeks towards
109 chondrogenic differentiation. As anticipated with the MSOD-B tissues, histological assessment revealed
110 the formation of a collagenous matrix (Masson's Trichrome) with cartilage features (Safranin-O, Figure
111 1D). Similarly, a successful chondrogenic differentiation and deposition of glycosaminoglycans could be
112 observed in the MSOD-BΔV1 (Figure 1D) constructs. A quantitative assessment (blyscan assay) confirmed
113 the comparable content in glycosaminoglycans in MSOD-B and VEGF-edited clones (Figure 1E).
114 Importantly, VEGF quantification in corresponding pellets validated the successful knockout of the
115 protein, barely detectable in the MSOD-BΔV1 and ΔV2 tissues (47.64 pg/pellet in edited clones versus
116 552.7 pg/pellet in MSOD-B, Figure 1F).

117 To further examine the potential impact of VEGF-editing on tissue formation, we performed
118 immunostaining analysis of the engineered cartilages. Confocal microscopy revealed strong deposition of
119 Collagen Type I (COL1) and Collagen Type X (COLX) in all samples, characteristic of mature hypertrophic
120 cartilage tissues (Figure 1G). However, while the immunostaining revealed the VEGF deposition in the
121 MSOD-B ECM, the protein could not be detected in the MSOD-BΔV1 samples (Figure 1G)

122 Taken together, this data indicates the successful generation of MSOD-B lines knocked-out in VEGF. The
123 MSOD-BΔV1 clones exhibited frank cartilage formation capacity with minimal level of VEGF. This validates
124 the use of CRISPR/Cas9 as a precision tool to edit the composition of cartilage tissue.

125

126 **VEGF knockout cartilage tissues retain bone remodeling capacity despite reduced early-stage**
127 **vascularization.**

128 To evaluate the functional impact of VEGF knockout in engineered constructs, we assessed both the
129 angiogenic and bone formation assays. Since the two clones exhibited similar in vitro tissue formation
130 capacity, only the MSOD-BΔV1 was selected for further performance assessment.

131 We first performed the Chorioallantoic Membrane (CAM) assay as ex vivo assessment of angiogenic
132 potential (Figure 2A). This assay provides insights into the biological activity and neovascularization
133 potential of each construct, through quantitative evaluation of vascular density around engineered grafts
134 After 4 days, we observed an extensive vessel formation in the periphery of both MSOD-B and MSOD-
135 BΔV1 eECMs (Figure 2B). Quantification of vascular densities [29] suggested a reduced vessel formation in
136 MSOD-BΔV1 samples but without reaching significance (Figure 2C and Supplementary Figure 2A). Thus,
137 the CAM assay indicated that both MSOD-B and MSOD-BΔV1 cartilages retain angiogenic potentials.

138 We next investigate in vivo the impact of the VEGF knockout on the graft capacity to undergo
139 endochondral ossification, by implanting cartilage grafts subcutaneously in an immunodeficient mouse
140 model. Importantly, prior to implantation, tissues were lyophilized using a pre-established protocol[21]. This
141 allowed us to assess the performance of the generated tissue itself, in line with the idea of developing off-
142 the-shelf substitutes. Samples were extracted after two and six weeks as early and late development
143 timepoints (Figure 2D). After two weeks in vivo, we first evaluated the angiogenic potential of tissues by
144 quantitative confocal microscopy imaging of 100 µm thick sections stained for CD31, a well-defined
145 vascular marker. This allowed us to evidence a dense vascular network in MSOD-B constructs, covering
146 the entirety of the grafts (Figure 2E). Instead, MSOD-BΔV1 displayed a more limited vascularization, pre-
147 dominantly at the tissue periphery (Figure 2E). Quantification confirmed these observations with MSOD-
148 B exhibiting a significantly higher volume of vessels per total section volume (0.523 μm^3 versus 0.231 μm^3
149 for MSOD-B and MSOD-BΔV1 respectively, Figure 2F).

150 Using microtomography, we further assessed the amount of mineralized tissue formed in a temporal
151 fashion. At two weeks, the formation of a cortical ring could already be observed in both MSOD-B and
152 MSOD-BΔV1 tissues (Figure 2G). Quantifications revealed a similar bone/mineralized volume normalized
153 to the total volume of the graft (BV/TV, Figure 2H, supplementary figure 2C and 2D) with 17 % and 16 %
154 in MSOD-B and MSOD-BΔV1 samples respectively. At the six-week timepoint, trabecular structures could

155 be observed in reconstructed 3D scans from both groups (Figure 2G). Remarkably, histological analysis
156 confirmed the similar development of the tissues with frank bone formation (Masson´s trichrome) already
157 at two weeks post-implantation and minimal remnants of cartilage (Safranin O) (Figure 2I). At six weeks
158 both samples remodeled into fully mature bone organs, characterized by presence of cortical and
159 trabecular structures as well as a bone marrow tissue filling the cavity (Figure 2I).

160 These results indicate that the absence of VEGF in cartilage tissue can delay the early vascularization of
161 MSOD-BΔV samples. However, this did not prevent nor impact the remodeling of the lyophilized grafts
162 into bone and bone marrow tissues indicating that VEGF is non-essential in order to efficiently instruct
163 endochondral ossification.

164

165 **RUNX2 knockdown does not prevent chondrogenic differentiation but impairs hypertrophy.**

166 We next investigated whether the composition and thus function of a graft could be modified by editing
167 transcriptional factors involved in mesenchymal cell differentiation. Using CRISPR/Cas9, we thus targeted
168 the RUNX2, a known master regulator particularly important for chondrocyte differentiation and
169 hypertrophy[30,31]. We designed gRNAs targeting the coding regions involved in cell signaling integration,
170 activation, and inhibition domain which are conserved in both isoforms of RUNX2 (Figure 3A,
171 Supplementary Figure 3A).

172 One gRNA was designed for targeting exon 2 (RUNX2_2.1), one targeting exon 5 (RUNX2_5.1), two
173 targeting exon 6 (RUNX2_6.1 and RUNX2_6.2) and one targeting exon 8 (RUNX2_8.1). Similar to the VEGF
174 set-up, gRNAs were transfected in MSOD-B cells together with a pU6-(BbsI)_CBh-Cas9-T2A-mCherry
175 plasmid to ensure transfection efficiency and single cell sorting of positive clones. Out of 385 single clones,
176 62 could be successfully expanded, corresponding to a 16.1% efficiency. From these clones, five were
177 derived from the RUNX2_5.1 gRNA, 18 from RUNX2_6.1, 15 from RUNX26.2 and 24 from RUNX2_8.1.

178 To identify successfully edited clones, we first screened for those exhibiting a decrease in their RUNX2
179 protein expression using intra cellular flow cytometry. Among the 62 clones, 17 displayed a reduced
180 RUNX2 pattern as compared to the MSOD-B control (Figure 3B and Supplementary Figure 3B) and were
181 further sent for sequencing analysis. This led to the identification of two successfully edited clones,
182 demonstrating a point mutation in the exon 6 of RUNX2 gene (Supplementary Figure 3C). To confirm the
183 knockout impact on the transcription factor structure, a Western Blot analysis was conducted on cellular
184 extracts of in vitro cultured cells. MSOD-B cells exhibited intact RUNX2 proteins of 52 – 62 kDa[32,33](Figure

185 3C). Instead, the RUNX2-edited cells displayed truncated versions of 32 – 42 kDa, consistent with the
186 expected mRNA shortening.

187 These two clones were defined as MSOD-BΔR1 and MSOD-BΔR2 and further assessed for their ability to
188 form cartilage in vitro. Following 3D chondrogenic differentiation, samples were processed for histological
189 analysis. The presence of cartilage structures embedded in a rich collagenous matrix could be observed in
190 all MSOD-B, MSOD-BΔR2 (Figure 3D) and MSOD-BΔR1 tissues (Supplementary Figure 3D). Quantification
191 of glycosaminoglycans revealed a similar content in all the groups (Figure 3E, Supplementary Figure 3E).
192 Using immunostaining combined with quantitative confocal microscopy, the possible impact of RUNX2-
193 editing on tissue hypertrophy was further investigated. First, Collagen Type II (COL2) staining confirmed
194 the similar distribution of cartilage matrix across MSOD-B, MSOD-BΔR1 and MSOD-BΔR2 samples (Figure
195 3F and Supplementary Figure 3F). However, we observed a clear distinction in the Collagen Type X (COLX)
196 expression pattern, a specific marker of hypertrophy which was hardly detectable in MSOD-BΔR tissues
197 (Figure 3F and Supplementary Figure 3F). Subsequent quantification confirmed a significant reduction of
198 COLX volume in MSOD-BΔR1 (0.236 μm^3) and MSOD-BΔR2 (0.182 μm^3) compared to MSOD-B (0.81 μm^3)
199 (Figure 3G, Figure 3H, Supplementary figure 3G-H-I).

200 To further characterize the functional impact of the RUNX2 knock-down, the MSOD-B and MSOD-BΔR1
201 osteogenic differentiation capacity was assessed in vitro. After 3 weeks of culture in osteogenic medium
202 (or expansion medium, control), Alizarin Red staining revealed a s a marked absence of mineralization in
203 MSOD-BΔR1 culture, while in stark contrast with MSOD-B cells (Figure 3I). Quantitative PCR analysis
204 indicated a lower expression of COLX and ALPL in MSOD-BΔR1 (Figure 3J), key osteogenic-associated
205 genes, of interest, the expression level of RUNX2 was only partially decreased in MSOD-BΔR1, in line with
206 the truncated mRNA reducing but not abrogating qPCR primers binding probability.

207 In summary, we here report the successful RUNX2 knockout in MSOD-B lines using CRISPR/Cas9. RUNX2
208 did not impair chondrogenesis but prevented the tissue hypertrophy, as well as the osteogenic potential
209 of the cells.

210 **RUNX2 knockout in cartilage tissues disrupts effective ectopic bone formation.**

211 To assess the corresponding impact of RUNX2-edited cartilages on bone formation, MSOD-B tissues (as
212 control) and MSOD-BΔR1 were lyophilized and implanted subcutaneously in immunodeficient mice for
213 two to six weeks. From microtomography image reconstructions, we observed an evident reduction of
214 mineralization in MSOD-BΔR1 compared to MSOD-B (Figure 4A) already after two weeks. This qualitative

215 and visual difference in mineralization persisted after six weeks in vivo (Figure 4A). Subsequent
216 quantifications confirmed these observations with a clear reduction in BV/TV as early as week 2 (16.46 %
217 in MSOD-B and 7.01 % in MSOD-BΔR1) and persisting at week 6 (20.03% in MSOD-B and 4.25 % in MSOD-
218 BΔR1) (Figure 4B). Histological analysis revealed an early bone formation at two weeks in both samples,
219 but to a lower extent in the MSOD-BΔR1 group (Figure 4C). As anticipated, MSOD-B tissues underwent full
220 remodeling after six weeks in vivo. In sharp contrast, the MSOD-BΔR1 only displayed a partial maturation
221 with limited presence of bone and bone marrow.

222 Altogether, this indicates an incomplete remodeling of RUNX2 edited samples with significantly delayed
223 cortical and trabecular structure formation. This correlates with the impaired hypertrophic phenotype in
224 the corresponding in vitro samples.

225 **RUNX2 knockout in cartilage tissues leads to better cartilage regeneration in a rat osteochondral defect.**

226 In order to assess the performance of CRISPR-Cas9 edited eECMs in a relevant skeletal regenerative
227 context, a proof-of-concept study in the rat osteochondral defect was performed. MSOD-B and MSOD-
228 BΔR1 tissues were lyophilized and placed in sub-chondral defect in the distal femur of a rat. The defect
229 consisted in a drill hole of 1mm diameter and 2mm depth (Figure 5A and supplementary figure 5A).
230 Positive controls consisted of untreated healthy rats.

231 Following explantation, histological stainings and micro-tomography were performed on all sample
232 groups. Hematoxylin and Eosin (H&E) and Masson's Trichrome indicated de novo bone formation in the
233 defect area for both the MSOD-B and MSOD-BΔR1 groups (Figure 5B and supplementary figure 5B). The
234 presence of fibrotic tissue as well as a reduced marrow compartment suggested an incomplete
235 remodeling at that timepoint (Figure 5B). Upon Tartrate-resistant acid phosphatase (TRAP) staining, we
236 observed elevated level osteoclastic activities in MSOD-B samples compared to MSOD-BΔR1 indicating
237 reduced rate of active bone formation in MSOD-BΔR1 (Figure 5C). The micro-CT quantification revealed a
238 30% repair of the damaged bone in the defect for both MSOD-B and MSOD-BΔR1 groups (Figure 5D,
239 Supplementary figure 5C). Of interest, a significantly higher trabecular separation was observed in MSOD-
240 B and MSOD-BΔR1, confirming an ongoing bone remodeling process (Figure 5E).

241 While no statistical differences in bone formation could be identified between the two groups, the MSOD-
242 BΔR1 tissue led to a superior regeneration of the cartilage area, as revealed by Safranin-O staining (Figure
243 5F) in the chondral zone (Figure 5F, a,b and c magnification). Interestingly, the MSOD-BΔR1 group
244 exhibited a higher remnants of GAGs in the subchondral area (Figure 5F, d,e and f magnification).

245 Quantification of cartilage tissue within condyle surface area confirmed a poor-to-no repair in the MSOD-
246 B group (1.05%, Figure 5G). In sharp contrast, the MSOD-BΔR1 implanted eECMs initiated a chondral
247 regeneration reaching approximately 20.67% of the total healthy cartilage area. The integration and
248 regeneration potential of engineered constructs was further evaluated by performing a semi-quantitative
249 histological assessment following a pre-existing grading system[34] (Table 1 and Supplementary table 1).
250 This approach allows for the systematic evaluation of critical repair tissue parameters, offering a
251 comparative measure of the regenerative efficacy of the engineered constructs against healthy tissue
252 benchmarks. In the assessment of stained femur condyle sections, cellular morphology and matrix staining
253 of the MSOD-BΔR1 group (66% and 50%, respectively) were significantly better compared to the MSOD-
254 B one (33% and 16%, respectively). Although both constructs exhibited reduced cartilage thickness and
255 subchondral bone regeneration, MSOD-BΔR1 consistently outperformed the MSOD-B grafts (33.33%
256 versus 8.33% and 25% versus 16.66%). Surface regularity and integration with adjacent cartilage also
257 revealed better outcomes in MSOD-BΔR1 (41% and 50%) as opposed to MSOD-B (50% and 33%), further
258 indicating an enhanced regenerative potential of the MSOD-BΔR1 constructs.

259 In conclusion, while both grafts yielded comparable bone regeneration within the osteochondral defects,
260 the RUNX2 deletion in cartilage grafts led to a superior cartilage regeneration.

261

262 **Discussion**

263 We here report the possibility to edit the composition and function of eECM by CRISPR/Cas9 engineering
264 of human mesenchymal lines. VEGF knockout led to successful in vitro formation of cartilage with targeted
265 protein depletion. Upon implantation, this impacted the graft vascularization onset but not the
266 endogenous instruction of the endochondral program. In turn, RUNX2 knockout prevented cartilage
267 hypertrophy in vitro, significantly delaying ectopic bone and bone marrow formation in vivo. This strategy
268 was validated in a functional osteochondral defect model, whereby prevention of cartilage hypertrophy
269 by RUNX2 deletion led to superior cartilage regeneration.
270 A clear interdependency of angiogenesis and osteogenesis occurs upon bone formation[35,36]. For this
271 reason, VEGF-enrichment has been naturally proposed as a strategy to accelerate or increase bone graft
272 vascularization[37,38]. Our study demonstrates that VEGF knocked-out cartilage templates retained full
273 osteoinductive potential in a challenging ectopic environment. Those results are in sharp contrast with
274 intramembranous strategies[39,40], including our previous work[19], whereby grafts remain insufficient in

275 promoting complete bone remodeling even upon VEGF-enrichment. This suggests that the first stage of
276 host progenitor recruitment by our eECM is not VEGF dependent, although subsequent tissue
277 vascularization and remodeling may be orchestrated in a second step by endogenous cell secretion. Other
278 pro-angiogenic proteins embedded in the matrix may also have compensated for the lack of VEGF, such
279 as BMP-2[20] known to stimulate endothelial cell proliferation, migration, and differentiation[41,42].
280 Conversely, RUNX2 deletion was shown to fully prevent cartilage hypertrophy, in line with published
281 mouse models also reporting a lack of endochondral ossification and lethality at birth upon RUNX2
282 knockout[43,44]. Here, MSOD-BΔR cartilage templates still exhibited frank bone formation capacity, but with
283 cortical and trabecular structures largely reduced as compared to controls. Future work may clarify if this
284 strictly results from the absence of COLX, or if an additional specific cartilage matrix component (e.g.
285 matrix metalloproteinases) impaired the instruction of endochondral ossification.
286 The performance in a regenerative context was further evaluated in a rat osteochondral defect model[45].
287 We defined an early timepoint of 3-week as providing the opportunity to assess the early contribution of
288 the grafts to both the cartilage and bone tissue regeneration. Strikingly, only the MSOD-BΔR could
289 contribute to a superior chondrogenesis. We hypothesize that the absence of hypertrophic features
290 prevented the template degradation and favored its integration to native cartilage. Despite the repair
291 performance being limited to an approximate 20% of native cartilage restoration, this is remarkable in
292 light of the BMP-2 content in our ECM prompting endochondral ossification [46,47,48]. In fact, preventing the
293 in vivo remodeling of engineered cartilage templates remains challenging in the skeletal regeneration
294 field, with bone marrow MSCs (BM-MSCs) cartilage systematically reaching hypertrophy and subsequent
295 ossification. Our results warrant further studies comprising additional timepoints to decipher the repair
296 dynamic, as well as the long-term stability of newly formed tissue. It also prompts a comparison with other
297 recently proposed *off-the-shelf* strategies, based on ECM[49] or synthetic scaffold materials[50], in order to
298 comprehend the feasibility to exploit our grafts for stable cartilage / joint repair[51,52]. Taken together, while
299 the relevance of CRISPR/Cas9 eECMs in cartilage repair remains to be further validated, our study
300 demonstrates the relevance of genetically-edited ECMs in regenerative contexts.

301 CRISPR/Cas9 editing of human mesenchymal cells has previously been explored for gene and cell therapy
302 applications[53,54] , for tailoring the immunomodulatory and/or differentiation capacity of engineered cells.
303 However, no studies have described the exploitation of editing strategies for the generation of eECMs,
304 whereby modified cells are absent from the final grafting product. Our work illustrate that this can be
305 achieved by direct targeting of secreted factors typically embedded upon ECM deposition, as

306 demonstrated with VEGF. Alternatively, we also propose the knockout of key transcription factors as a
307 strategy for custom eECM generation by impacting their tissue developmental/maturation stages.
308 A clear implication of our work lies in the possibility to decipher the necessary factors capable of
309 instructing de novo tissue formation. Those findings will be of high relevance for the design of eECMs
310 tailored in composition. Beyond bone repair, our study also bears high relevance in other regenerative
311 contexts. In fact, an exciting opportunity also lies in harnessing CRISPR/Cas9 for editing eECMs and tuned
312 their immunogenicity. Key inflammatory components could be turned down, leading to improved efficacy
313 of repair in line with the immuno-engineering principles[55,56] .
314 Importantly, our study describes the exploitation of eECMs in a lyophilized form, thus conferring an off-
315 the-shelf storage solution. Together with the standardization of production conferred by stable cell
316 sources, our concept offers exciting translational opportunities. In fact, instrumental to this work is the
317 use of dedicated hMSC lines. The genetic modification of primary cells is laborious, and their limited
318 lifespan ex vivo challenges their selection, characterization, and exploitation for tissue engineering
319 applications[57,58]. Here, the MSOD-B was harnessed as an unlimited cell source with robust differentiation
320 potential. Nonetheless, the editing of eECMs remains tedious in part due to the limited CRISPR/Cas9
321 efficiency and potential off-target effects, calling for a systematic clonal selection. In addition, while large
322 CRISPR/Cas9 screening can be performed in other stem cell systems[59,60], the critical cell mass required for
323 effective cartilage formation affects parallelization and leads to limited throughput. Nonetheless, after
324 the identification and characterization process, the resulting cell lines can be banked and used for
325 unlimited tissue manufacturing.
326 The MSOD-B line remains the only human cell source capable of priming endochondral ossification by
327 engineering living or cell-free grafts. This was demonstrated to be driven by the combined low dose of
328 BMP-2 embedded in the tissue (~40 ng/tissue) together with glycosaminoglycans and other thousands of
329 identified ECM proteins[20]. The BMP-2 amount is thus far below the typical amount used in sECMs
330 approaches for effective osteoinduction, falling in the microgram to milligram range[21]. This is one key
331 advantage of eECM graft, exhibiting a biological complexity that so far has not been matched by sECMs.
332 Ideally, the two approaches are complementary as the editing of eECMs could inform on the necessary
333 but sufficient factors driving effective regeneration. Those would in turn be embedded in a sECMs strategy
334 and offer a fast and possibly cost-effective solution.
335 To conclude, the present work offers a platform for decoding factors involved in tissue regeneration and
336 generate tailored eECM. Here, illustrated in the context of skeletal repair, our study may offer similar
337 opportunities in other regenerative situations.

338

339 **Materials and Methods:**

340 **Cell expansion**

341 MSOD-B cells and their modified progeny were cultured in a humidified incubator at 37 °C and 5% CO_2
342 using complete medium consisting of α-minimum essential medium (αMEM) supplemented with 10%
343 fetal bovine serum, 1% HEPES, 1% sodium pyruvate, 1% penicillin-streptomycin-glutamine solution, and 5
344 ng/ml of fibroblast growth factor-2 (FGF-2) (all from Gibco). Cells were seeded at a density of 3200
345 cells/cm^2 until they reached 90% confluency. The medium was replaced twice a week.

346 **Chondrogenic and osteogenic differentiation**

347 MSOD-B cells and their modified progeny were harvested from culture flasks by adding Trypsin-EDTA
348 (0.25%) (Gibco) and subsequently seeded on cylindrical Collagen Type I scaffold (Avitene™ Ultrafoam™
349 Collagen Sponge, Davol) of 6 mm in diameter and 3 mm in thickness at a density of 2 x 10^6 cells per scaffold
350 in 12 well plates coated with 1 % agarose (Sigma) for chondrogenic differentiation and in a 12-well plate
351 for osteogenic differentiation. Tissue constructs were cultured for three weeks in chondrogenic medium
352 (DMEM supplemented with 1% penicillin-streptomycin-glutamine, 1% HEPES (1M), 1% sodium pyruvate
353 (100 mM), 1% ITS (100x) (Insulin, Transferrin, Selenium) (all from Gibco), 0,47 mg/ml linoleic acid (Sigma),
354 0.12% bovine serum albumin (25 mg/mL) (BSA) (Sigma), 0.1 mM ascorbic acid (Sigma), 10^{-7} M
355 dexamethasone (Sigma) and 10 ng/ml TGF-β3 (Novartis)). The cells in the 12 well plates were
356 supplemented for three weeks with osteogenic (or expansion medium, control) differentiation medium
357 (α-minimum essential medium (αMEM) with 10% fetal bovine serum, 1% HEPES (1M), 1% sodium pyruvate
358 (100 x 10^{-3}M) and 1% penicillin-streptomycin-glutamine solution (100X), supplemented with 0.01M β-
359 dexamethasone and 0.1M ascorbic acid). Media were replaced twice a week.

360 **Lyophilization**

361 After three weeks of chondrogenic differentiation, the tissue constructs were rinsed twice with PBS 7.2
362 (without calcium/magnesium Gibco), snap frozen in liquid nitrogen for five minutes and then lyophilized
363 using a freeze dryer (Labconco) (-80 °C and 0.05 mbar) overnight. Thereafter, the lyophilized tissue
364 constructs were stored at 4 °C.

365 **Transfection of MSOD-B cells with gRNAs**

366 MSOD-B cells were seeded at a density of 400,000 cells per well in 12 well plates to reach a minimum of
367 80% confluency the following day. The medium was replaced before transfection. The transfection was
368 performed with a / ratio of 2 µL lipofectamine to 1 µg DNA. A DNA mix was prepared for each of the five
369 gRNAs and the two plasmid controls. DNA mixtures were composed of 1 µg of plasmid, 2 µL of P3000

370 reagent and 50 µL of OptiMEM (Thermo-Fischer). A lipofectamine cocktail was prepared for all DNA
371 mixtures consisting of 24 µL of lipofectamine 3000 in 400 µL of OptiMEM. Lipofectamine and the DNA
372 mixtures were added at a 1:1 ratio. After 48h, cells were analyzed and mCherry positive clones were FACS
373 sorted as single cells in 96-well plates using ARIAIII (BD Biosciences). Successfully expanded clones were
374 then further characterized.

375 **ELISA**

376 VEGF protein content was measured in supernatant collected from cells seeded at 570 cells/cm^2 in T175
377 flask and cultured for 3 days. Content from engineered cartilage tissues was assessed following digestion
378 in RIPA buffer. The Quantikine ELISA kit for Human VEGF-A Immunoassay from the R&D System was used
379 according to the manufacturer instructions to determine protein concentration.

380 **Intracellular flow cytometry**

381 MSOD-B and MSOD-B ΔRUNX2 cells were trypsinized, fixed and permeabilized using the
382 Fixation/Permeabilization Kit (BD Biosciences). Following a blocking step in 10% normal donkey serum
383 (Sigma), cells were stained with a primary antibody against RUNX2 (Rabbit anti-human, Thermo-Fischer
384 PA5-82787) for one hour at room temperature. After primary antibody incubation, cells were washed and
385 stained with an Allophycocyanin (APC) labeled secondary antibody (Donkey anti-rabbit IgG DyLight™ 649,
386 Biolegend 406406) for 30-45 minutes at room temperature in 2% normal donkey serum. The Control
387 samples consisted of unstained cells (negative control) and cells incubated only with the secondary
388 antibody (secondary Ab control). Data were recorded on a BD LSRFortessa™ Cell Analyzer (BD
389 Biosciences). FCS files were analyzed using the FlowJo™ software (FlowJo LLC, 10.5.3, BD Biosciences).

390 **Western blotting**

391 MSOD-B and MSOD-B ΔRUNX2 cells were trypsinized and washed with ice cold PBS twice and lysed on ice
392 for 10 min in RIPA buffer (#10017003, Thermo Fisher Scientific) supplemented with 1× proteinase and
393 phosphatase inhibitor cocktail (#78440, Thermo Fisher Scientific). The lysates were centrifuged at 16,
394 000*g* for 15 min +4 °C, and the supernatants were collected. Sample buffer (Laemmli buffer (#161-0737,
395 BioRad) supplemented with 5% 2-mercaptoethanol, 1× proteinase and phosphatase inhibitor cocktail
396 (#78440, Thermo Fisher Scientific) was added to the supernatant at 1:1 ratio. Samples were boiled at 95
397 °C for 5 minutes and stored at −80 °C or kept on ice until gel loading. Proteins were separated using Bolt
398 gels according to manufacturer's protocol (#NW04122, #B0002, Thermo Fisher Scientific). iBlot2 system
399 was used to transfer the proteins on polyvinylidene fluoride membrane (PVDF) membrane according to
400 manufacturer's protocol (#IB24001, Thermo Fisher Scientific). PVDF membrane was washed once in 1×
401 PBST buffer (#28352, Thermo Fisher Scientific) and blocked in 2% blocking solution (#10156414, Thermo

402 Fisher Scientific) for 1 h at room temperature. Membranes were incubated overnight at +4 °C with primary
403 antibodies at recommended concentrations in 1% blocking solution. Membranes were washed three
404 times (5 min for each wash) with 1× PBST buffer, and secondary HRP-conjugated antibodies in 1% blocking
405 solution were added to the membranes at 1:5000 concentration for 1 h incubation at room temperature.
406 Membranes were washed three times with 1× PBST and proteins were detected by chemiluminescence
407 according to manufacturer's protocol (#RPN2232, Thermo Fisher Scientific). The following antibodies
408 were used. primary antibodies: RunX– (D1L7F - 12556) from Cell Signaling Technology and Actin (612656)
409 is from Becton Dickinson. The secondary antibodies were anti-Mouse (GENA931) from Sigma-Aldrich, anti-
410 Rabbit (NA9340V) from Thermo Fisher Scientific.

411 **Biochemical analysis (GAG analysis)**

412 Lyophilized tissue constructs were digested by overnight incubation in 0.5 ml of Proteinase K solution (1
413 mg/mL Proteinase K, Sigma; 10 ug/ml pepstatin A, Sigma; 1 mM EDTA, Sigma; 100 mM Iodoacetamide;
414 50mM Tris) at pH 7.6 and 56 °C. The GAG content of digested samples was analyzed using
415 Glycosaminoglycan Assay Blyscan kit (Biocolor) following the manufacturer instruction.

416 **Mice**

417 FoxN1 KO BALB/C (nude mice) 6–8-weeks old, were obtained from Charles River Laboratories. All mouse
418 experiments and animal care were performed in accordance with the Lund University Animal Ethical
419 Committee guidelines (ethical permit #M15485–18). Mice were housed at a 12-hour light cycle in
420 individually ventilated cages at a positive air pressure and constant temperature. Mice were fed with
421 autoclaved diet and water ad libitum. During the implantation procedure, anaesthesia was performed
422 with 2-3 % Isoflurane (Attane). The mice were kept on a heating pad during the procedure to avoid the
423 heat loss.

424 **Micro-CT scanning**

425 In vivo samples were explanted and fixed overnight with 4% formaldehyde before ex vivo micro-CT
426 analysis using a U-CT system (MILABS, Netherland) equipped with a tungsten x-ray source at 50 kV and
427 0.21 mA. Volumes were reconstituted at 10 µm isotropic voxel size. For total volume (TV) analysis, each
428 sample was assessed with Blender (v2.82a, Netherland). Briefly, a mesh was created surrounding the 3D
429 reconstruction of each sample and the volume occupied was then quantified. For bone volume (BV)
430 analysis, the highly mineralized tissue volume was quantified using Seg3D (v2.2.1, NIH, NCRR, Science
431 Computing and Imaging Institute (SCI))

432 **Sample preparation for histological analysis.**

433 In vitro samples were directly fixed prior to sectioning. In vivo samples were fixed and subsequently
434 decalcified with a 10% EDTA solution, pH = 8, at 4 °C for two weeks prior to tissue embedding.
435 Paraffin embedding was performed on samples fixed in 4% formalin (Solveca AB). Tissues were
436 dehydrated by immersion in consecutive solutions of 35%, 70%, 95%, and 99.5% graded ethanol solution
437 (Solveco AB). Immersion in a 99.5% ethanol/xylene solution (1:1, Fisher Scientific) was then performed
438 for ten minutes followed by two rinsing in xylene (Fisher Scientific) for 20 minutes. Subsequently,
439 tissues were embedded in paraffin at 56 °C overnight, before sectioning with a microtome (Microm HM
440 355 Rotary Microto–e) in 5 - 10 µm sections. The sections were then dried overnight at 37 °C before
441 staining. Prior to staining, sections were deparaffinized by two washes in xylene for 7 minutes and once
442 in 99.5% ethanol/xylene solution (1:1) for 3 minutes. Afterwards, sections were hydrated twice in
443 consecutive solutions of 99.5%, 95%, 70%, and 35% ethanol, for 7 minutes each.

444 Agarose embedding was performed on samples fixed overnight with 4% paraformaldehyde (Thermo
445 Scientific), using 4% low-melting agarose (Sigma). Sections of 100 µm thickness were obtained using a
446 7000smz vibratome (Campden) with stainless steel or ceramic blades.

447 **Safranin O Staining**

448 Paraffin-embedded sections were stained using Mayer's hematoxylin solution (Sigma-Aldrich) for 10
449 minutes. Samples were then placed under running distilled water to remove superfluous staining from
450 the sections. Subsequently, sections were stained with 0.01% fast green solution (Fisher Scientific) for five
451 minutes and rinsed with 1% acetic acid solution (glacial, Fisher Scientific) for 15 seconds. After that, the
452 slides were stained with 0.1% safranin O (Fisher Scientific) solution for 5 minutes. Dehydration and
453 clearing were performed by immersion in 95%, 99.5% ethanol, 99.5% ethanol/xylene solution (1:1) and
454 xylene twice successively for 2 minutes. Finally, the stained slides were mounted with glass slides using
455 PERTEX mounting medium (PERTEX, HistoLab).'

456 **Masson's trichrome staining**

457 Masson's trichrome staining was performed using the trichrome staining kit (Sigma-Aldrich Sweden AB)
458 according to the manufacturer's guidelines. Briefly, tissue sections were deparaffinized and immersed in
459 cold running deionized water for 3 minutes. Then the sections were kept in Bouin's solution at room
460 temperature overnight or at 56 °C for 15 minutes. The slides were washed by running tap water and
461 stained using working Weigert's iron hematoxylin solution (Sigma) for five minutes for nuclei detection
462 (in black). After washing the slides, the cytoplasm was stained in red with Biebrich Scarlet-Acid fuchsin for
463 five minutes followed by clearing the slides by immersion in working phosphotungstic/ phosphomolybdic
464 acid solution for five minutes. Collagen stained blue by immersion in aniline blue solution for five minutes

465 followed by clearing in 1% acetic acid (glacial, Fisher Scientific) solution diluted in distilled water (glacial,
466 Fisher Scientific) for two minutes and washing with running deionized water. Finally, the sections were
467 dehydrated in graded ethanol solutions (95% once, 100% twice) for two minutes each before washing
468 with xylene twice for two minutes and mounted with PERTEX mounting medium.

469 **Hematoxylin and Eosin staining**

470 Paraffin-embedded sections were stained using Mayer's hematoxylin solution (Sigma-Aldrich) for 10
471 minutes. Samples were then placed under running distilled water to remove superfluous staining from
472 the sections. The slides were immersed precisely in 1X phosphate-buffered saline (PBS) for 1 minute to
473 intensify the blue nuclei staining while preserving tissue integrity. Following this, a thorough rinse with 3
474 changes of distilled water effectively removed any residual PBS, preparing the sections for the subsequent
475 counterstaining step. Subsequently, Alcoholic-Eosin (Sigma-Aldrich) was applied for 1 minute as the
476 counterstain without any rinsing post-application, ensuring optimal interaction of the staining solution
477 with the tis. Dehydration and clearing were performed by immersion in 95%, 99.5% ethanol, 99.5%
478 ethanol/xylene solution (1:1) and xylene twice successively for 2 minutes. Finally, the stained slides were
479 mounted with glass coverslips using PERTEX mounting medium (PERTEX, HistoLab).

480 **Quantitative PCR**

481 Total RNA isolation was conducted from in vitro engineered tissues utilizing the Quick-RNA extraction kit
482 (Zymo Research, R1055) following the manufacturer's protocol. Subsequently, cDNA extraction was
483 carried out using cDNA synthesis kit (Invitrogen 11917020). The quantitative real-time polymerase chain
484 reaction (qRT-PCR) was performed, utilizing the assay on demand from Applied Biosystems to assess the
485 expression of specific genes. These genes include glyceraldehyde 3-phosphate dehydrogenase (GAPDH,
486 HS02786624_G1), runt-related transcription factor 2 (Runx2, Hs00231692_m1), alkaline phosphatase
487 (ALP, Hs01029144_m1), and collagen type X (ColX, Hs00166657_m1).

488 **Rat osteochondral defect model**

489 Ten- to 12-week-old male Sprague Dawley rats (n=11) were purchased from JANVIER LABS
490 (France). After 7 days of acclimation the rats were anesthetized using 3% isoflurane. Then,
491 animals were placed on a 37°C warm heating pad in prone position. Once anesthetized, isoflurane
492 was lowered to 2 to 2.5%, and buprenorphine (Temgesic, 30 µg/kg; Indivior Europe Ltd., Dublin,
493 Ireland) was injected subcutaneously for analgesia. The right hind limb of the animal was shaved
494 and carefully disinfected, and an incision was made along the skin and soft tissue to expose the
495 right knee. After cleaning the knee laterally from soft tissue, patella was displaced laterally to

496 expose the distal femur. An articular cartilage defect with 2mm depth and 1mm diameter was
497 created at the trochlear groove of femur. The defect was then push-fitted with the grafts, and
498 not secured with any sutures. The wound was closed in a layered fashion using resorbable sutures
499 (Vicryl 45-0, Ethicon, Somerville, USA) by closing the joint capsule, followed by the muscle tissue
500 (continuous interlaced suture), followed by closing the skin (Donati suture). Animals started load
501 bearing immediately after surgery. After 3 weeks (n=11) animals were anesthetized by isoflurane
502 inhalation (3%), followed by CO2 asphyxiation, and right-femur were harvested prior to
503 subsequent micro-CT and histological characterization.

504 **Histology grading method**

505 Histological sections from rat femur condyles were stained with Safranin-O, Masson's trichrome, and H&E
506 staining. A semi-quantitative analysis of the repaired tissue was performed by utilizing a customized
507 adaptation of the histological grading system initially outlined by Wakitani et al[61]. This modified scale
508 encompasses six distinct parameters: cellular morphology, matrix staining, surface regularity, cartilage
509 thickness, regenerated subchondral bone formation, and integration with neighbouring cartilage. Each
510 parameter was graded on a numerical scale ranging from 0 to 4 points by independent expert observers,
511 where a maximum total score of 16 indicates the presence of tissue displaying characteristics akin to
512 entirely healthy and normal tissue (Table 1).
513

514 **Cartilage quantification method**

515 An evaluation of three distinct sites within the condyle defect was conducted to ascertain the proportion
516 of cartilage in each knee. Utilizing the measured femoral condyle thickness (200µm) and defect length
517 (1mm), a standardized Region of Interest (ROI) was defined using ImageJ. The percentage of cartilage-
518 positive regions within each defect was calculated in relation to the total ROI size, offering a quantitative
519 assessment of cartilage regeneration. This identical approach was applied to evaluate the percentage of
520 cartilage in the healthy control samples.
521

522 **Trabecular thickness (Tb.Th) and trabecular separation (Tb.Sp)**

523 Image analysis was performed by ImageJ. To evaluate the defect space, a rectangular interface region
524 (2 × 1 mm) was defined as the Region of Interest . Trabecular thickness (Tb.Th) and trabecular separation
525 (Tb.Sp),was calculated inside the ROI using BoneJ plugin.
526

527 **Vascular density quantification**

528 To assess vascular density, the Quantitative Vascular Analysis Tool (Q-VAT)[29] was utilized. The samples
529 were placed inside the chicken egg for CAM assay, and the images were acquired using a digital
530 microscope. These images were then segmented into tiles for detailed analysis. The binary vascular masks
531 were generated using the Q-VAT's automated capabilities, to distinguish vascular structures within the
532 tissue. The tool then facilitated the separation of vessel measurements based on their diameters, allowing
533 for a differentiated quantification of macro- and microvasculature. These binary masks were then
534 processed to calculate the vascular density, which refers to the proportion of the tissue area occupied by
535 vessels. This quantitative metric was evaluated for each tile, and the mean vascular density was computed
536 across all tiles for each tissue sample. As part of the analysis, we applied Q-VAT to double or triple-stained
537 slides to quantify the overlapping percentage of vessels, comparing various time points to observe
538 changes over the course of the experiment.

539

540 **Immunofluorescence**

541 Agarose-embedded sections were treated with 0.5% Triton X-100 (Sigma) in PBS supplemented with 20%
542 donkey serum (Jackson ImmunoResearch) for one hour at room temperature (RT) for blocking and
543 permeabilization. After blocking/permeabilization, sections were stained with primary antibodies (mouse
544 anti-Collagen II (Invitrogen, MA137493), Anti-Collagen 1 (Abcam, ab138492), VEGF polyclonal antibody
545 (Bioss Antibodies, bs-0279R), rabbit anti-Collagen Type X (ColX) (abbexa, abx101469), Goat anti
546 mouse/rat CD31 (R&D system, YZU0119121), VEGF at 4 °C overnight. Sections were washed three times
547 using cold PBS with 0.1% Triton X-100, 20 minutes each, followed by staining with secondary antibodies
548 (CF568 donkey anti-rabbit (Biotium, 20098), CF567 anti-goat (Invitrogen, A11057), CF633 donkey anti-
549 mouse (Sigma-Aldrich, SAB4600131 in 2% donkey serum for three hours at room temperature. Sections
550 were washed three times using cold PBS with 0.1% Triton X-100, 20 minutes each once more.
551 All sections were mounted using the Vectashield antifade mounting medium containing DAPI (Vector
552 Laboratories, H1200). A LSM780 confocal microscope (Zeiss) with a 10x/20x objective was used to capture
553 images and image series of whole tissue sections (z-step = 2 µm). The IMARIS 9.5 software package (Oxford
554 Instruments) was used to analyze the data.

555

556 **Acknowledgements**

557 We express our gratitude to the following institutions and individuals for their invaluable support and
558 contributions to this study: Lund University, Medical Faculty, FACS Facility (Anna Hammarberg), Cell and

559 Gene Therapy core facility (Pia Johansson) and Imaging Facility at Lund Stem Cell Centre, as well as the
560 Lund University Bioimaging Centre, for providing access to the X-ray CT system. The funding for this
561 research was made possible by a Knut and Alice Wallenberg grant, the Medical Faculty at Lund University,
562 the Swedish Research Council, the European Research Council (Starting grant hOssicle #948588 to P.E.B),
563 and Region Skåne. Figures were generated using BioRender.com. Special thanks to Ani Grigoryan and
564 Dimitra Zacharaki for their expertise and valuable insights regarding FACS experiments, and to Steven
565 Dupard for his advice and guidance on the design of gRNAs and molecular techniques. Christian Hansen
566 deserves our appreciation for providing the mcherry plasmid and offering valuable guidance and
567 knowledge related to CRISPR-Cas9.

568

569

570 **References**

571 1. Bonnans C, Chou J, Werb Z. Remodelling the extracellular matrix in development and disease.
572 *Nat Rev Mol Cell Biol*. 2014;15(12):786-801. doi:10.1038/nrm3904

573 2. Hussey GS, Dziki JL, Badylak SF. Extracellular matrix-based materials for regenerative medicine.
574 *Nat Rev Mater*. 2018;3(7):159-173. doi:10.1038/s41578-018-0023-x

575 3. Fattahi R, Chamkhorami FM, Taghipour N, Keshel SH. The effect of extracellular matrix
576 remodeling on material-based strategies for bone regeneration: Review article. *Tissue Cell*.
577 2022;76(January):101748. doi:10.1016/j.tice.2022.101748

578 4. Mouw JK, Ou G, Weaver VM. Extracellular matrix assembly: A multiscale deconstruction. *Nat Rev*
579 *Mol Cell Biol*. 2014;15(12):771-785. doi:10.1038/nrm3902

580 5. Assunção M, Dehghan-Baniani D, Yiu CHK, Später T, Beyer S, Blocki A. Cell-Derived Extracellular
581 Matrix for Tissue Engineering and Regenerative Medicine. *Front Bioeng Biotechnol*.
582 2020;8(December):1-10. doi:10.3389/fbioe.2020.602009

583 6. Hinderer S, Layland SL, Schenke-Layland K. ECM and ECM-like materials - Biomaterials for
584 applications in regenerative medicine and cancer therapy. *Adv Drug Deliv Rev*. 2016;97:260-269.
585 doi:10.1016/j.addr.2015.11.019

586 7. Hinderer S, Layland SL, Schenke-Layland K. ECM and ECM-like materials - Biomaterials for
587 applications in regenerative medicine and cancer therapy. *Adv Drug Deliv Rev*. 2016;97:260-269.
588 doi:10.1016/j.addr.2015.11.019

589 8. Fattahi R, Chamkhorami FM, Taghipour N, Keshel SH. The effect of extracellular matrix
590 remodeling on material-based strategies for bone regeneration: Review article. *Tissue Cell*.
591 2022;76(January):101748. doi:10.1016/j.tice.2022.101748

592 9. Tang G, Liu Z, Liu Y, et al. Recent Trends in the Development of Bone Regenerative Biomaterials.
593 *Front Cell Dev Biol*. 2021;9(May):1-18. doi:10.3389/fcell.2021.665813

594 10. Gao C, Peng S, Feng P, Shuai C. Bone biomaterials and interactions with stem cells. *Bone Res*.
595 2017;5(May):1-33. doi:10.1038/boneres.2017.59

596 11. Filippi M, Born G, Chaaban M, Scherberich A. Natural Polymeric Scaffolds in Bone Regeneration.
597 *Front Bioeng Biotechnol*. 2020;8(May). doi:10.3389/fbioe.2020.00474

598 12. Reddy MSB, Ponnamma D, Choudhary R, Sadasivuni KK. A comparative review of natural and
599 synthetic biopolymer composite scaffolds. *Polymers (Basel)*. 2021;13(7).
600 doi:10.3390/polym13071105

601 13. Decaris ML, Leach JK. Design of experiments approach to engineer cell-secreted matrices for
602 directing osteogenic differentiation. *Ann Biomed Eng*. 2011;39(4):1174-1185.
603 doi:10.1007/s10439-010-0217-x

604 14. Harvestine JN, Orbay H, Chen JY, Sahar DE, Leach JK. Cell-secreted extracellular matrix,
605 independent of cell source, promotes the osteogenic differentiation of human stromal vascular
606 fraction. *J Mater Chem B*. 2018;6(24):4104-4115. doi:10.1039/c7tb02787g

607 15. Hoch AI, Mittal V, Mitra D, Vollmer N, Zikry CA, Leach JK. Cell-secreted matrices perpetuate the
608 bone-forming phenotype of differentiated mesenchymal stem cells. *Biomaterials*. 2016;74:178-
609 187. doi:10.1016/j.biomaterials.2015.10.003

610 16. Haumer A, Bourgine PE, Occhetta P, Born G, Tasso R, Martin I. Delivery of cellular factors to
611 regulate bone healing. *Adv Drug Deliv Rev*. 2018;129:285-294. doi:10.1016/j.addr.2018.01.010

612 17. Sadr N, Pippenger BE, Scherberich A, et al. Enhancing the biological performance of synthetic
613 polymeric materials by decoration with engineered, decellularized extracellular matrix.
614 *Biomaterials*. 2012;33(20):5085-5093. doi:10.1016/j.biomaterials.2012.03.082

615 18. Prewitz MC, Seib FP, von Bonin M, et al. Tightly anchored tissue-mimetic matrices as instructive
616 stem cell microenvironments. *Nat Methods*. 2013;10(8):788-794. doi:10.1038/nmeth.2523

617 19. Bourgine PE, Gaudiello E, Pippenger B, et al. Engineered Extracellular Matrices as Biomaterials of
618 Tunable Composition and Function. *Adv Funct Mater*. Published online 2017.
619 doi:10.1002/adfm.201605486

620 20. Pigeot S, Klein T, Gullotta F, et al. Manufacturing of Human Tissues as off-the-Shelf Grafts
621 Programmed to Induce Regeneration. *Advanced Materials*. 2021;33(43).
622 doi:10.1002/adma.202103737

623 21. Pigeot S, Klein T, Gullotta F, et al. Manufacturing of Human Tissues as off-the-Shelf Grafts
624 Programmed to Induce Regeneration. *Advanced Materials*. 2021;33(43).
625 doi:10.1002/adma.202103737

626 22. Grigoryan A, Zacharaki D, Balhuizen A, et al. Engineering human mini-bones for the standardized
627 modeling of healthy hematopoiesis, leukemia, and solid tumor metastasis. *Sci Transl Med*.
628 2022;14(666):1-16. doi:10.1126/scitranslmed.abm6391

629 23. Golchin A, Shams F, Karami F. Advancing Mesenchymal Stem Cell Therapy with CRISPR/Cas9 for
630 Clinical Trial Studies. In: *Cell Biology and Translational Medicine,*. Vol 8. ; 2019:89-100.
631 doi:10.1007/5584_2019_459

632 24. Hazrati A, Malekpour K, Soudi S, Hashemi SM. CRISPR/Cas9-engineered mesenchymal
633 stromal/stem cells and their extracellular vesicles: A new approach to overcoming cell therapy
634 limitations. *Biomedicine & Pharmacotherapy*. 2022;156:113943.
635 doi:10.1016/j.biopha.2022.113943

636 25. Geurts MH, Clevers H. CRISPR engineering in adult stem cell-derived organoids for gene repair
637 and disease modelling. 2023;1(January):32-45. doi:10.1038/s44222-022-00013-5

638 26. Hu K, Olsen BR. The roles of vascular endothelial growth factor in bone repair and regeneration.
639 *Bone*. 2016;91:30-38. doi:10.1016/j.bone.2016.06.013

640 27. Duda GN, Geissler S, Checa S, Tsitsilonis S, Petersen A, Schmidt-Bleek K. The decisive early phase
641 of bone regeneration. *Nat Rev Rheumatol*. 2023;19(February):78-95. doi:10.1038/s41584-022-
642 00887-0

643 28. Ran FA, Hsu PD, Wright J, Agarwala V, Scott DA, Zhang F. Genome engineering using the CRISPR-
644 Cas9 system. *Nat Protoc*. 2013;8(11):2281-2308. doi:10.1038/nprot.2013.143

645 29. Callewaert B, Gsell W, Himmelreich U, Jones EAV. Q-VAT: Quantitative Vascular Analysis Tool.
646 *Front Cardiovasc Med*. 2023;10. doi:10.3389/fcvm.2023.1147462

647 30. Otto F, Thornell AP, Crompton T, et al. Cbfa1, a candidate gene for cleidocranial dysplasia
648 syndrome, is essential for osteoblast differentiation and bone development. *Cell*. 1997;89(5):765-
649 771. doi:10.1016/S0092-8674(00)80259-7

650 31. Komori T, Yagi * H., Nomura S, Yamaguchi A. Targeted disruption of. *Proc Natl Acad Sci U S A*.
651 1998;95(15):8692-8697.

652 32. Kim HJ, Kim WJ, Ryoo HM. Post-Translational Regulations of Transcriptional Activity of RUNX2.
653 *Mol Cells*. 2020;43(2):160-167. doi:10.14348/molcells.2019.0247

654 33. Hattori EY, Masuda T, Mineharu Y, et al. A RUNX-targeted gene switch-off approach modulates
655 the BIRC5/PIF1-p21 pathway and reduces glioblastoma growth in mice. *Commun Biol*.
656 2022;5(1):1-11. doi:10.1038/s42003-022-03917-5

657 34. Maehara H, Sotome S, Yoshii T, et al. Repair of large osteochondral defects in rabbits using
658 porous hydroxyapatite/collagen (HAp/Col) and fibroblast growth factor-2 (FGF-2). *Journal of*
659 *Orthopaedic Research*. 2010;28(5):677-686. doi:10.1002/jor.21032

660 35. Kusumbe AP, Ramasamy SK, Adams RH. Coupling of angiogenesis and osteogenesis by a specific
661 vessel subtype in bone. *Nature*. 2014;507(7492):323-328. doi:10.1038/nature13145

662 36. Tuckermann J, Adams RH. The endothelium–bone axis in development, homeostasis and bone
663 and joint disease. *Nat Rev Rheumatol*. 2021;17(10):608-620. doi:10.1038/s41584-021-00682-3

664 37. Largo RD, Burger MG, Harschnitz O, et al. VEGF Over-Expression by Engineered BMSC Accelerates
665 Functional Perfusion, Improving Tissue Density and In-Growth in Clinical-Size Osteogenic Grafts.
666 *Front Bioeng Biotechnol*. 2020;8(July):1-13. doi:10.3389/fbioe.2020.00755

667 38. Yang YQ, Tan YY, Wong R, Wenden A, Zhang LK, Rabie ABM. The role of vascular endothelial
668 growth factor in ossification. *Int J Oral Sci*. 2012;4(2):64-68. doi:10.1038/ijos.2012.33

669 39. Burger MG, Grosso A, Briquez PS, et al. Robust coupling of angiogenesis and osteogenesis by
670 VEGF-decorated matrices for bone regeneration. *Acta Biomater*. 2022;149:111-125.
671 doi:10.1016/j.actbio.2022.07.014

672 40. Behr B, Tang C, Germann G, Longaker MT, Quarto N. Locally applied vascular endothelial growth
673 factor A increases the osteogenic healing capacity of human adipose-derived stem cells by
674 promoting osteogenic and endothelial differentiation. *Stem Cells*. 2011;29(2):286-296.
675 doi:10.1002/stem.581

676 41. Zuo WH, Zeng P, Chen X, Lu YJ, Li A, Wu J Bin. Promotive effects of bone morphogenetic protein 2
677 on angiogenesis in hepatocarcinoma via multiple signal pathways. *Sci Rep*. 2016;6(July):1-9.
678 doi:10.1038/srep37499

679 42. Lowery JW, de Caestecker MP. BMP signaling in vascular development and disease. *Cytokine*
680 *Growth Factor Rev*. 2010;21(4):287-298. doi:10.1016/j.cytogfr.2010.06.001

681 43. Kamekura S, Kawasaki Y, Hoshi K, et al. Contribution of runt-related transcription factor 2 to the
682 pathogenesis of osteoarthritis in mice after induction of knee joint instability. *Arthritis Rheum*.
683 2006;54(8):2462-2470. doi:10.1002/art.22041

684 44. Komori T, Yagi * H., Nomura S, Yamaguchi A. Targeted disruption of. *Proc Natl Acad Sci U S A*.
685 1998;95(15):8692-8697.

686 45. Meng X, Ziadlou R, Grad S, et al. Animal Models of Osteochondral Defect for Testing Biomaterials.
687 *Biochem Res Int*. 2020;2020. doi:10.1155/2020/9659412

688 46. Sekiya I, Vuoristo JT, Larson BL, Prockop DJ. In vitro cartilage formation by human adult stem cells
689 from bone marrow stroma defines the sequence of cellular and molecular events during
690 chondrogenesis. *Proc Natl Acad Sci U S A*. 2002;99(7):4397-4402. doi:10.1073/pnas.052716199

691 47. Pelttari K, Winter A, Steck E, et al. Premature induction of hypertrophy during in vitro
692 chondrogenesis of human mesenchymal stem cells correlates with calcification and vascular
693 invasion after ectopic transplantation in SCID mice. *Arthritis Rheum*. 2006;54(10):3254-3266.
694 doi:10.1002/art.22136

695 48. Mueller MB, Tuan RS. Functional characterization of hypertrophy in chondrogenesis of human
696 mesenchymal stem cells. *Arthritis Rheum*. 2008;58(5):1377-1388. doi:10.1002/art.23370

697 49. Browe DC, Burdis R, Díaz-Payno PJ, et al. Promoting endogenous articular cartilage regeneration
698 using extracellular matrix scaffolds. *Mater Today Bio*. 2022;16. doi:10.1016/j.mtbio.2022.100343

699 50. Steele JAM, Moore AC, St-Pierre JP, et al. In vitro and in vivo investigation of a zonal
700 microstructured scaffold for osteochondral defect repair. *Biomaterials*. 2022;286.
701 doi:10.1016/j.biomaterials.2022.121548

702 51. Park DY, Min BH, Park SR, et al. Engineered cartilage utilizing fetal cartilage-derived progenitor
703 cells for cartilage repair. *Sci Rep*. 2020;10(1):1-13. doi:10.1038/s41598-020-62580-0

704 52. Zeng J, Huang L, Xiong H, et al. Injectable decellularized cartilage matrix hydrogel encapsulating
705 urine-derived stem cells for immunomodulatory and cartilage defect regeneration. *NPJ Regen*
706 *Med*. 2022;7(1):1-12. doi:10.1038/s41536-022-00269-w

707 53. Golchin A, Shams F, Karami F. Advancing Mesenchymal Stem Cell Therapy with CRISPR/Cas9 for
708 Clinical Trial Studies. In: *Cell Biology and Translational Medicine,*. Vol 8. ; 2019:89-100.
709 doi:10.1007/5584_2019_459

710 54. Hazrati A, Malekpour K, Soudi S, Hashemi SM. CRISPR/Cas9-engineered mesenchymal
711 stromal/stem cells and their extracellular vesicles: A new approach to overcoming cell therapy
712 limitations. *Biomedicine & Pharmacotherapy*. 2022;156:113943.
713 doi:10.1016/j.biopha.2022.113943

714 55. Chen Z, Klein T, Murray RZ, et al. Osteoimmunomodulation for the development of advanced
715 bone biomaterials. *Materials Today*. 2016;19(6):304-321. doi:10.1016/j.mattod.2015.11.004

716 56. Xie Y, Hu C, Feng Y, et al. Osteoimmunomodulatory effects of biomaterial modification strategies
717 on macrophage polarization and bone regeneration. *Regen Biomater*. 2020;7(3):233-245.
718 doi:10.1093/rb/rbaa006

719 57. Aamodt JM, Grainger DW. Extracellular matrix-based biomaterial scaffolds and the host
720 response. *Biomaterials*. 2016;86:68-82. doi:10.1016/j.biomaterials.2016.02.003

721 58. Ramakrishnaiah Siddappa, Ruud Licht, Clemens van Blitterswijk J de B. Donor variation and loss of
722 multipotency during in vitro expansion of human mesenchymal stem cells for bone tissue
723 engineering. *Journal of Orthopaedic Research*. 2007;25(8).

724 59. LaFleur MW, Nguyen TH, Coxe MA, et al. A CRISPR-Cas9 delivery system for in vivo screening of
725 genes in the immune system. *Nat Commun*. 2019;10(1):1-10. doi:10.1038/s41467-019-09656-2

726 60. Bock C, Datlinger P, Chardon F, et al. High-content CRISPR screening. *Nature Reviews Methods*
727 *Primers*. 2022;2(1). doi:10.1038/s43586-021-00093-4

728 61. Maehara H, Sotome S, Yoshii T, et al. Repair of large osteochondral defects in rabbits using
729 porous hydroxyapatite/collagen (HAp/Col) and fibroblast growth factor-2 (FGF-2). *Journal of*
730 *Orthopaedic Research*. 2010;28(5):677-686. doi:10.1002/jor.21032

731

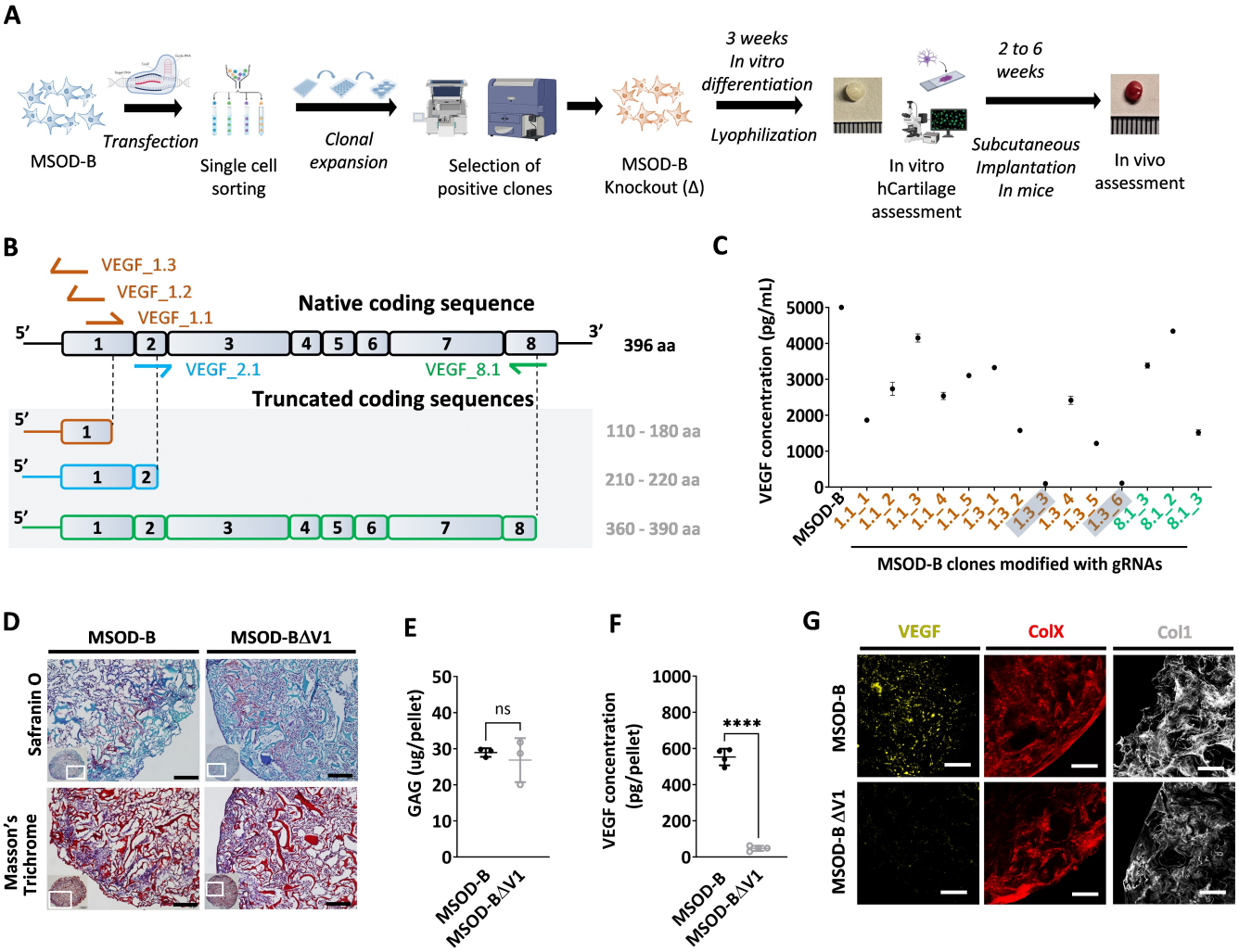

Figure 1. CRISPR/Cas9 editing of mesenchymal cell lines lead to efficient VEGF knockout in cartilage tissues. A) Experimental scheme depicting the generation of CRISPR/Cas9-edited MSOD-B lines, and the subsequent in vitro and in vivo tissue formation assessment. B) Overview of the native human VEGF coding sequence composed of eight exons. Designed gRNAs and their targeted binding sites are illustrated, as well as the corresponding expected impact on the coding sequence. gRNAs targeting exon 1 (orange) disrupt translation initiation and inhibit protein expression, gRNA targeting exon 2 (blue) disrupts VEGF receptor binding, and gRNA targeting exon 8 (green) alters the C-Terminal sequence and repress activation of protein. C) ELISA-based quantitative analysis of VEGF protein content in cell culture supernatant from expanded single cell colonies. From all clones, only two had no detectable level of VEGF (1.3_3 and 1.3_6). These clones were subsequently defined as MSOD-BΔV1 and MSOD-BΔV2. D) Histological assessment of in vitro differentiated constructs using Safranin O (top panel) and Masson's trichrome (bottom panel) stains. Both the MSOD-B and MSOD-BΔV1 displayed glycosaminoglycans (GAG) (orange to reddish in Safranin O) and collagen content (Blueish in Masson's trichrome), indicating successful cartilage formation (Scale bars = 200 µm). Left bottom inserts show the whole tissue section. E) Quantitative assessment of the total GAG content in MSOD-B and MSOD-BΔV1 in vitro differentiated constructs. Unpaired t-test, n = 3 biological replicates, n.s. = not significant. F) ELISA-based quantitative assessment of VEGF protein in in vitro differentiated constructs. Unpaired t-test, n = 3-4 biological replicates, ****$p < 0.0001$. G) Immunofluorescence images of MSOD-B and MSOD-BΔV1 tissues. Displayed images consist of 3D-stacks from 80-100 µm thick sections, stained for VEGF (yellow), Collagen Type X (COLX, red) and Collagen Type I (COL1, grey). A clear reduction in the VEGF signal could be observed in the MSOD-BΔV1 tissues, indicating a successful VEGF knockdown (Scale bars = 80 µm).

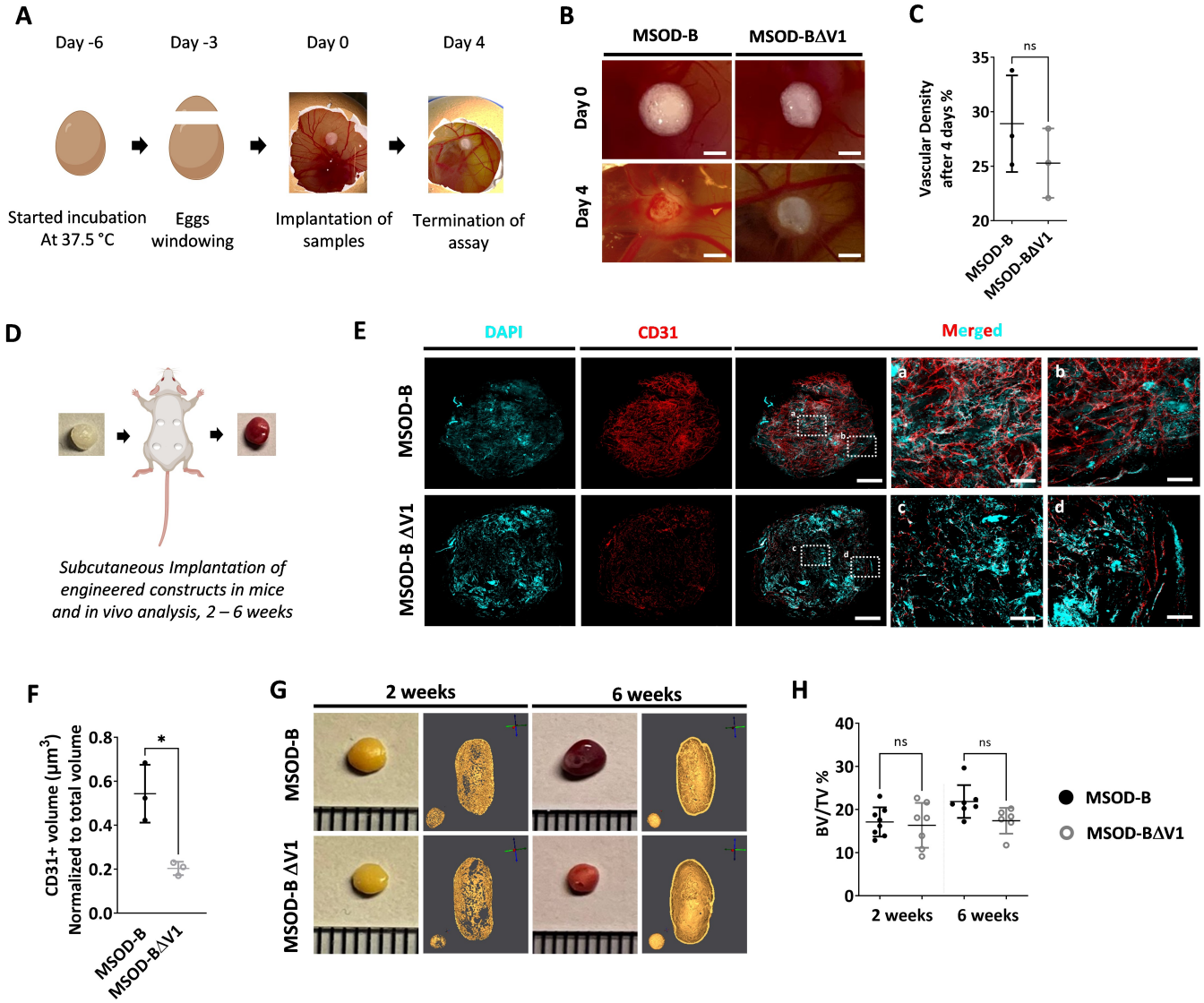
A
Day -6
Day -3
Day 0
Day 4
Started incubation At 37.5 °C
Eggs windowing
Implantation of samples
Termination of assay
B
MSOD-B
MSOD-BΔV1
Day 0
Day 4
C
Vascular Density after 4 days %
ns
MSOD-B
MSOD-BΔV1
D
Subcutaneous Implantation of engineered constructs in mice and in vivo analysis, 2 – 6 weeks
E
DAPI
CD31
Merged
MSOD-B
MSOD-B ΔV1
F
CD31+ volume (µm³) Normalized to total volume
*
MSOD-B
MSOD-BΔV1
G
2 weeks
6 weeks
MSOD-B
MSOD-B ΔV1
H
BV/TV %
ns
ns
2 weeks
6 weeks
MSOD-B
MSOD-BΔV1
I
2 weeks
6 weeks
Safranin O
Masson's Trichrome
Safranin O
Masson's Trichrome
MSOD-B
MSOD-BΔV1
CB
BM
TB

Figure 2. VEGF knockout cartilage tissues retain bone remodeling capacity despite reduced early-stage vascularization

A) Experimental scheme of the Chorioallantoic Membrane (CAM) assay, for ex vivo evaluation of angiogenic potential. B) Macroscopic comparison of in vitro MSOD-B and MSOD-BΔV1 constructs at day 0 (day of implantation) and day 4 (4 days post-implantation), illustrating robust de novo vessel formation perfusing the tissues (Scale bars at 1 mm). C) Quantitative Analysis of Vascular Density in MSOD-B and MSOD-BΔV1. Vascular densities were quantified from macroscopic images obtained on day 4 using ImageJ. Unpaired t-test, n = 3-4 biological replicates, n.s. = not significant. D) overview of the subcutaneous implantation procedure in mice and subsequent in vivo evaluation of vascularization from 2 to 6 weeks post-implantation. E) Immunofluorescence images of MSOD-B and MSOD-BΔV1 tissues two weeks post-in vivo implantation. Displayed images consist of 3D-stacks from 80-100 µm thick sections, vessels stained with mouse CD31 (red) and nuclei with DAPI (cyan) (Scale bars at 500 µm except for magnified white inserts at 80 µm). Box "a" and "c" display the periphery whereas Box "b" and "d" show the central region of MSOD-B and MSOD-BΔV1 constructs respectively. A reduction in tissue vascularization is observed in MSOD-BΔV1 samples. F) Quantitative analysis of the CD31 signal using an isosurface-based strategy (IMARIS software). Unpaired t-test, n = 3-4 biological replicates, *$p < 0.05$. G) Representative macroscopic and microtomography images of in vivo constructs retrieved at two and six weeks post-implantation. H) Microtomography-based quantification of the sample's bone/ mineralized volume over their total volume (ratio). No significant differences between MSOD-B and MSOD-BΔV1 could be observed. (BV: Bone Volume, TV: Total Volume). Ordinary One-way ANOVA, n=8 biological replicates, n.s.=not significant I) Histological analysis of in vivo tissues using Safranin O and Masson's trichrome stains, at two (2W) and six weeks (6W) post-implantation. Both sample types underwent full remodeling into a bone organ after 6 weeks, with presence of bone structures and a bone marrow compartment (Scale bars = 200 µm). CB – cortical bone; BM – bone marrow. TB – trabecular bone.

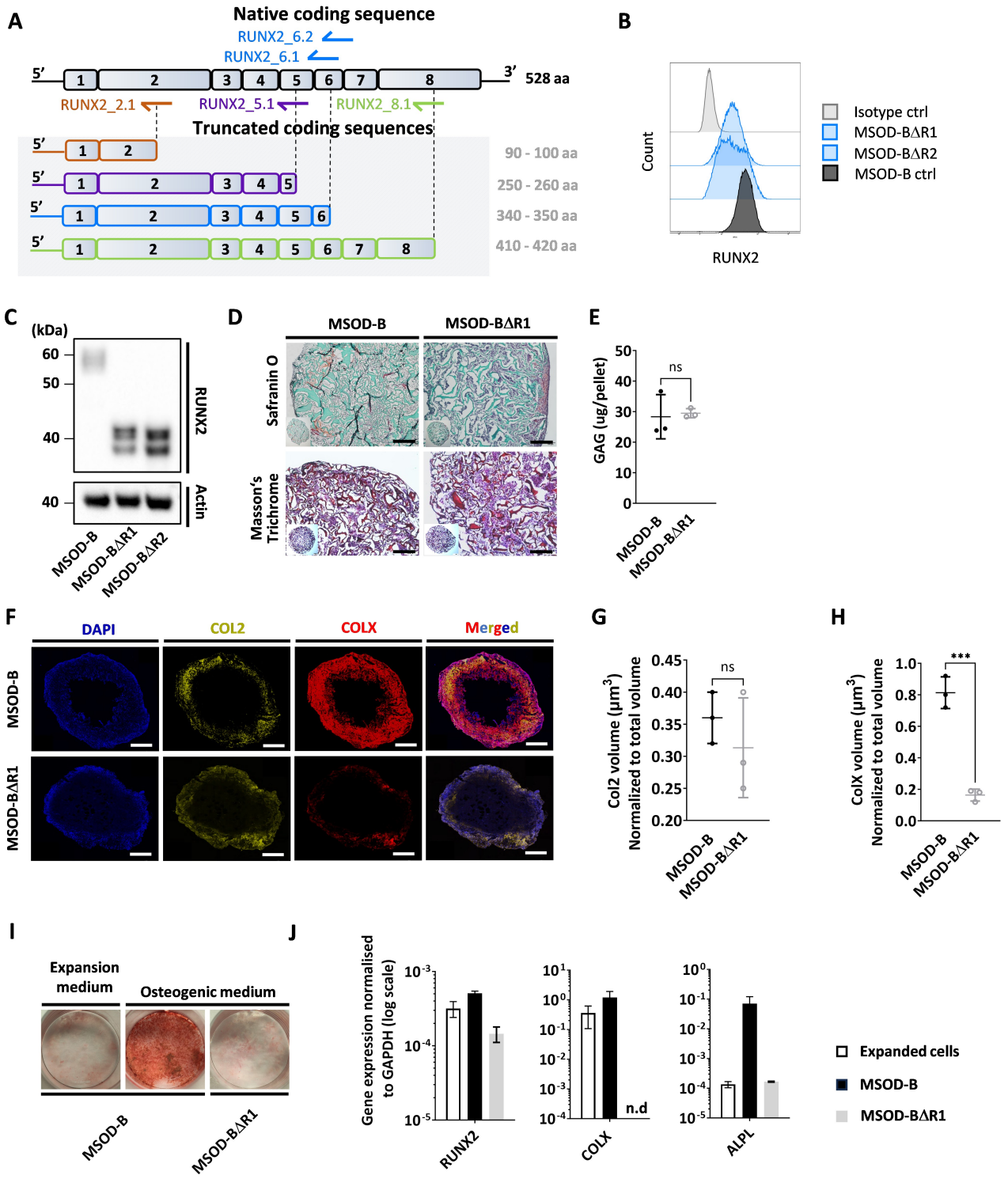
A
Native coding sequence
RUNX2_6.2
RUNX2_6.1
5'
1
2
3
4
5
6
7
8
3'
528 aa
RUNX2_2.1
RUNX2_5.1
RUNX2_8.1
Truncated coding sequences
90 - 100 aa
250 - 260 aa
340 - 350 aa
410 - 420 aa
B
Count
RUNX2
Isotype ctrl
MSOD-BΔR1
MSOD-BΔR2
MSOD-B ctrl
C
(kDa)
60
50
40
40
RUNX2
Actin
MSOD-B
MSOD-BΔR1
MSOD-BΔR2
D
MSOD-B
MSOD-BΔR1
Safranin O
Masson's Trichrome
E
GAG (ug/pellet)
ns
MSOD-B
MSOD-BΔR1
F
DAPI
COL2
COLX
Merged
MSOD-B
MSOD-BΔR1
G
Col2 volume (µm³) Normalized to total volume
ns
MSOD-B
MSOD-BΔR1
H
ColX volume (µm³) Normalized to total volume
***
MSOD-B
MSOD-BΔR1
I
Expansion medium
Osteogenic medium
MSOD-B
MSOD-BΔR1
J
Gene expression normalised to GAPDH (log scale)
n.d
RUNX2
COLX
ALPL
Expanded cells
MSOD-B
MSOD-BΔR1

Figure 3. RUNX2 knockout does not prevent chondrogenic differentiation but impairs hypertrophy A) Overview of the human RUNX2 coding sequence comprising 8 exons. gRNAs and their corresponding expected protein structure. The gRNA targeting exon 2 (orange) disrupts the DNA binding domain, gRNA targeting exon 5 (violet) disrupts nuclear translocation, gRNAs targeting exon 6 (blue) disrupt the transcriptional activation domain and gRNAs targeting exon 8 (green) disrupt the nuclear matrix targeting signal and repress the protein function. B) Intracellular flow cytometry for RUNX2 detection in MSOD-B and RUNX2-edited clones. A clear protein reduction could be observed in the 6.1_1 and 6.1_23 clones. C) Western blot analysis of RUNX2 in cultured MSOD-B and RUNX2-edited cells. The genetic editing of RUNX2 is confirmed by the detection of the truncated proteins. Actin is used as a control to normalize the protein content. D) Histological analysis of in vitro constructs using Safranin O (top) and Masson's trichrome (bottom) stains, indicating the presence of cartilage matrices (Scale bars = 200 µm). E) Quantitative assessment of the total GAG content in corresponding in vitro generated tissues. Unpaired t-test, n=3 biological replicates, n.s.=not significant. F) Immunofluorescence images of MSOD-B and MSOD-B∆R1 tissues. Displayed images consist of 3D-stacks from 80-100 µm thick sections, stained for DAPI (blue), Collagen Type II (COL2, yellow) and Collagen Type X (COLX, red). A clear reduction in the COLX signal could be observed in the MSOD-B∆R1 tissues, indicating impaired hypertrophy. (Scale bars = 500 µm) G) Isosurface-based quantification of the COL2 immunofluorescent signal using the IMARIS software. No significant difference between groups confirm the retention of cartilage formation in RUNX2-edited constructs. Unpaired t-test, n=3 biological replicates, n.s.=not significant. H) Isosurface-based quantification of the COLX immunofluorescent signal using the IMARIS software, confirming the disruption of hypertrophy in the MSOD-B∆R1 constructs. Unpaired t-test, n=3, ***$p < 0.001$, n.s. = not significant. I) Alizarin Red staining evidencing a lack of mineralization in the MSOD-B∆R1 culture compared to the MSOD-B. Two way ANOVA test, n=3, **$p < 0.01$, n.s. = not significant. J) Quantitative PCR analysis displaying the relative expression levels of osteogenesis-related genes: RUNX2, COL1, and ALPL. The expression is normalized to GAPDH as housekeeping gene. n.d= not detected.

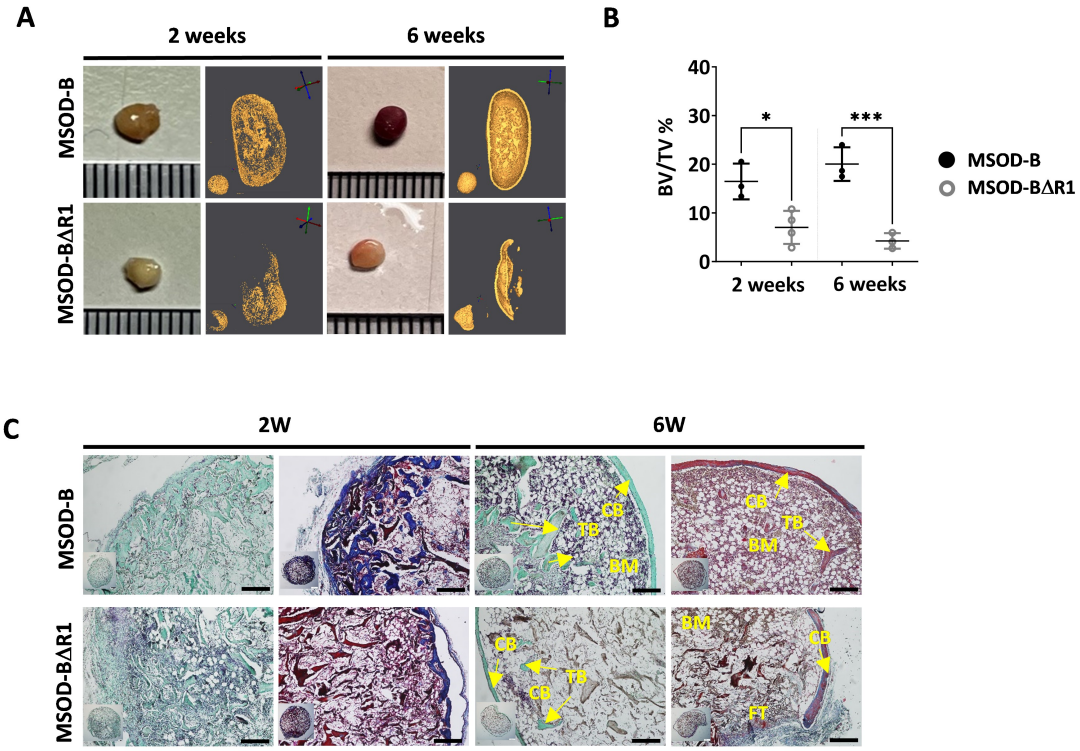

Figure 4. RUNX2 knockout in cartilage tissues disrupts effective ectopic bone formation A) Representative macroscopic and microtomography images of in vivo constructs retrieved at two and six weeks post-implantation. B) Microtomography-based quantification of the sample's bone/mineralized volume over their total volume (ratio). (BV: Bone Volume, TV: Total Volume). A marked difference is observed as early as two weeks, with a clear lower mineral content in MSOD-BΔR1 samples. Ordinary one way ANOVA, n=3 biological replicates, *$p < 0.05$, ***$p < 0.001$. C) Histological analysis of in vivo constructs using Safranin O and Masson's trichrome stains. After two weeks (2W), a higher bone formation is already evident in the MSOD-B control group. The MSOD-BΔR1 samples explanted after 6 weeks (6W) displayed presence of cortical and trabecular bone, but also large amount of fibrous tissue indicating an incomplete remodeling. (Scale bars = 200 µm).

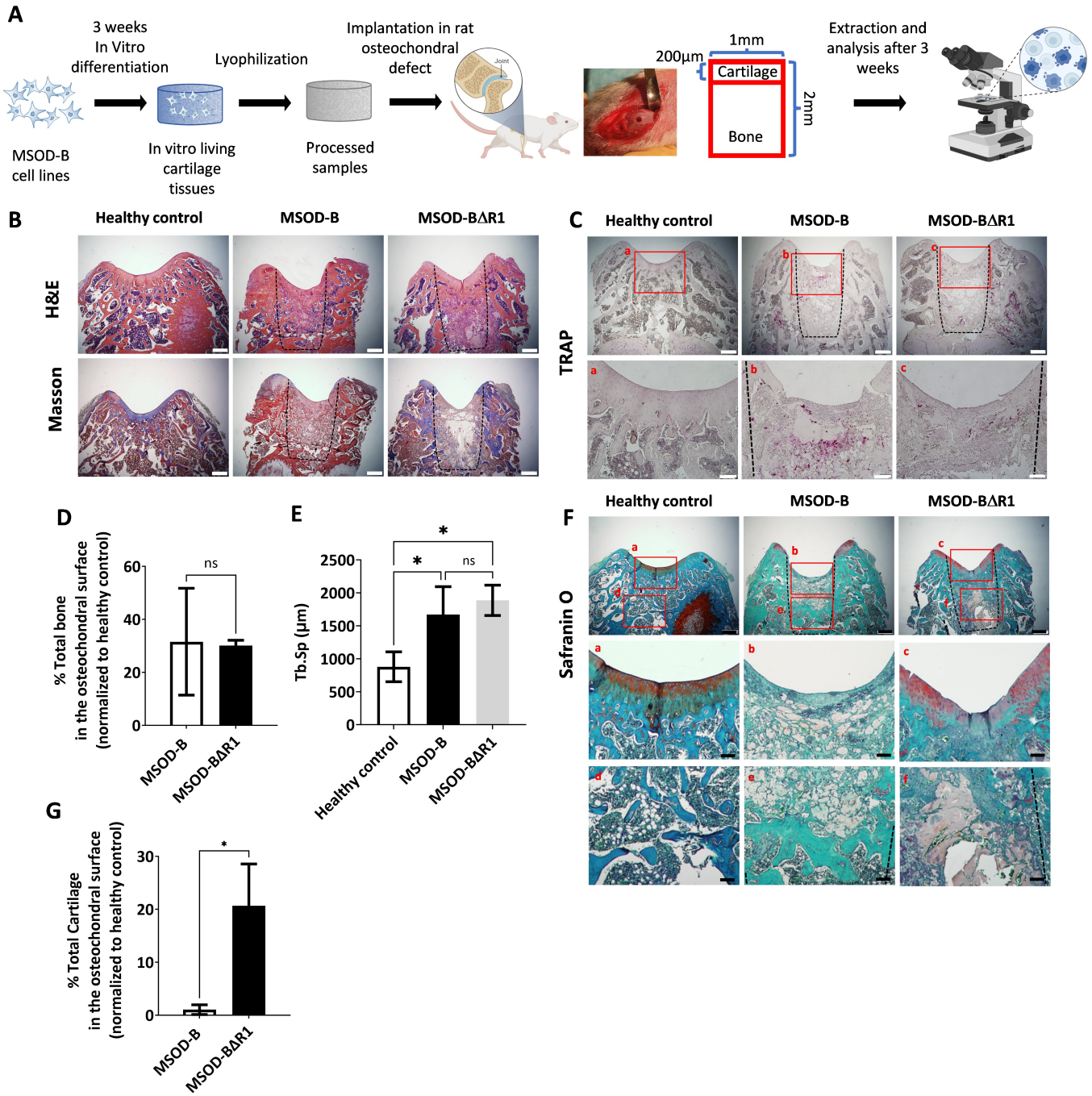

Figure 5. RUNX2 knockout in cartilage tissues leads to better cartilage regeneration and maintenance in osteochondral defect in rats A) Experimental scheme for the regenerative potential assessment of MSOD-B & MSOD-BΔR1 cartilage tissues in a rat osteochondral defect. B) Histological analysis of the osteochondral defects for each group using H&E and Masson's trichrome stains, at three weeks post-implantation. The dash-line marks the defect area. (Scale bars = 500 µm) C) Histological analysis the osteochondral defects using TRAP staining reporting osteoclastic activity, at three weeks post-implantation. The dash-line marks the defect area. (Scale bars = 500 µm and 100 µm for magnified areas) D) Microtomography-based quantification of the sample's total bone/mineralized volume normalized to the healthy control in percentage. Unpaired t-test, n=3 biological replicates, n.s.=not significant. E) Image J based quantification of Trabecular separation (Tb.Sp). One way ANOVA test, n=3 biological replicates, *$p < 0.05$ F) Histological analysis of the osteochondral defects using Safranin O staining. After three weeks, a higher regeneration of the surface cartilage is evident in the MSOD-BΔR1 group (Scale bars = 500 µm and 100 µm for magnified areas). The magnified regions of the subchondral area (d,e,f) show higher cartilage remnants in the MSOD-BΔR1 group. G) Quantitative analysis of cartilage regeneration in the osteochondral surface as compare to the healthy control (100%). Unpaired t-test, n=3 biological replicates, *$p < 0.05$.

Table 1: Scoring rate for individual categories

Semi-quantitative analysis utilizing a modified histological grading system, including parameters such as cellular morphology, matrix staining, surface regularity, thickness of cartilage, subchondral bone formation and integration of adjacent cartilage , resulting in a comprehensive assessment of tissue regeneration and integration

	Scoring Rate (%) (SD)					
	Cell Morphology	Matrix Staining	Surface Regularity	Thickness of Cartilage	Regenerated Subchondral Bone	Integration with Adjacent Cartilage
Healthy	100 (0)	100 (0)	100 (0)	100 (0)	100 (0)	100 (0)
MSOD-B	33,33 (28,86)	16,66 (14,43)	50 (0)	8,33 (14,33)	16,66 (14,33)	33,33 (14,33)
MSOD-B ΔR1	66,66 (14,33)	50 (0)	41,66 (14,33)	33,33 (28,86)	25 (25)	50 (0)

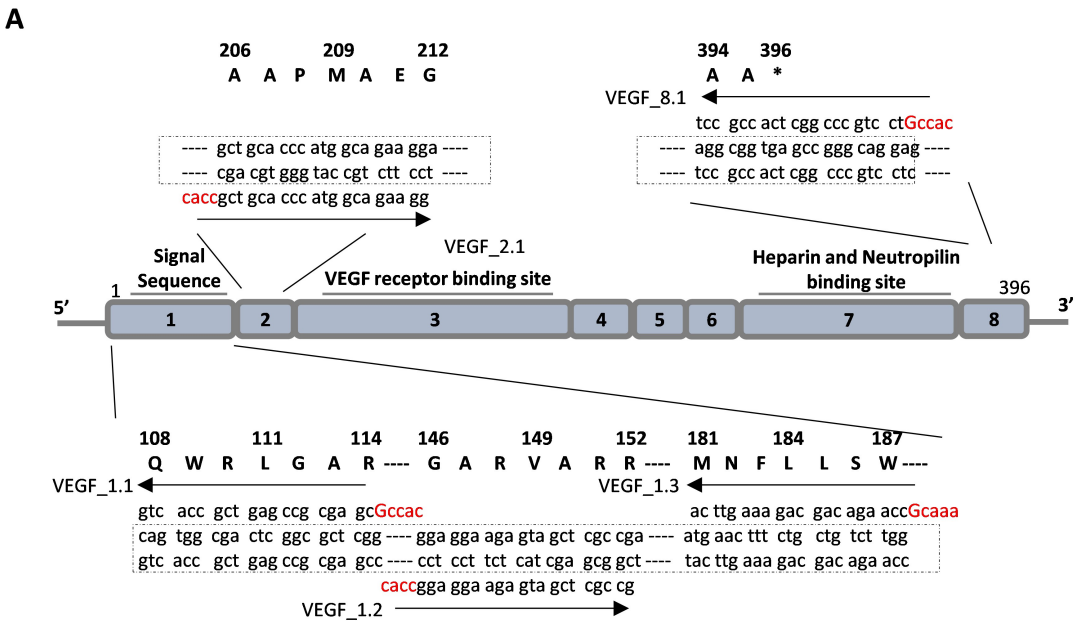

Supplementary figure 1. CRISPR/Cas9 editing of mesenchymal cell lines lead to efficient VEGF knockout in cartilage tissues A) Overview of the human VEGF exon structure, nucleotide sequences of targeting gRNAs and their corresponding amino acid sequences.

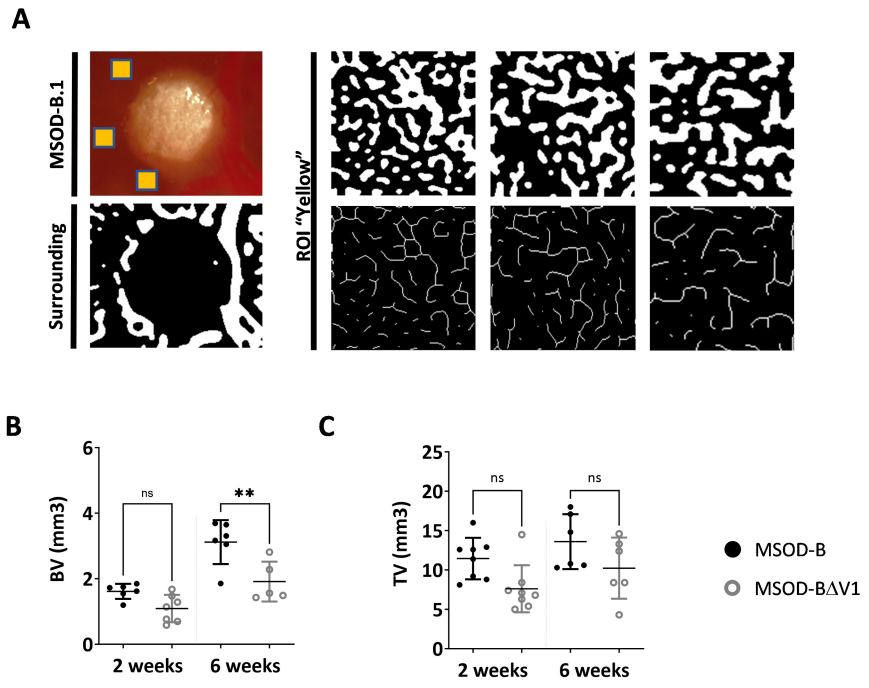

Supplementary figure 2. VEGF knockout cartilage tissues retain bone remodeling capacity despite reduced early-stage vascularization

A) Sequential processing of a vascular tissue section using Q-VAT, depicting the original image, binary mask creation, and vessel segmentation for quantitative vascular density analysis. B) Microtomography analysis (Bone/mineralized volume) showed significant differences between in vivo constructs at both two weeks and six weeks time points (One way ANOVA, n=3, **$p < 0.01$). C) Microtomography analysis (total volume) did not show significant difference between in vivo constructs at either two weeks or six weeks time points (One way ANOVA, n=3, n.s.= not significant) (BV: Bone Volume, TV: Total Volume).

A

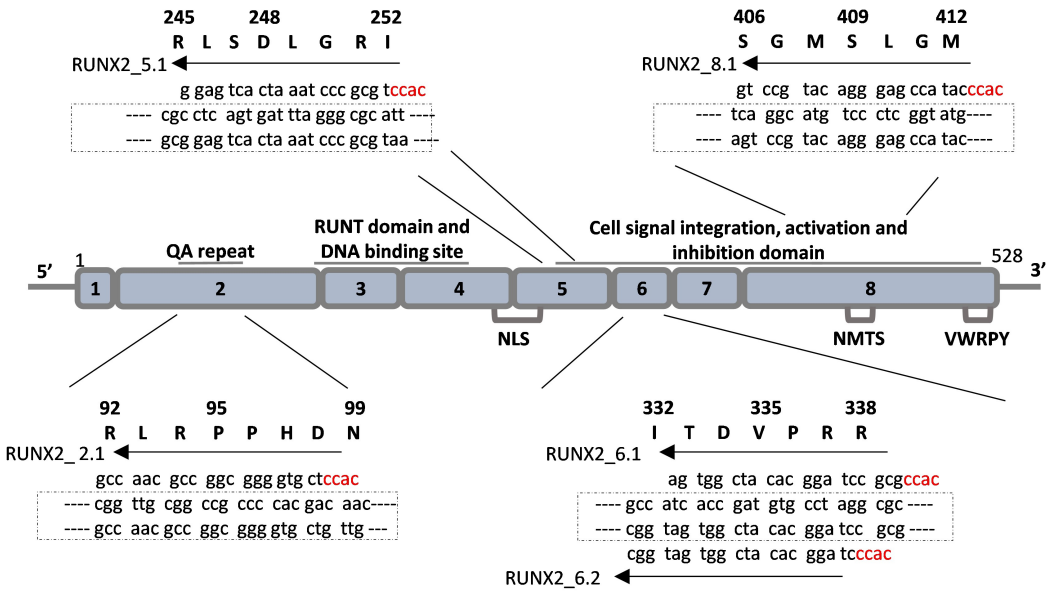
245 248 252
R L S D L G R I
RUNX2_5.1
g gag tca cta aat ccc gcg tccac
---- cgc ctc agt gat tta ggg cgc att ----
---- gcg gag tca cta aat ccc gcg taa ----
406 409 412
S G M S L G M
RUNX2_8.1
gt ccg tac agg gag cca tacccac
---- tca ggc atg tcc ctc ggt atg----
---- agt ccg tac agg gag cca tac----
RUNT domain and DNA binding site
Cell signal integration, activation and inhibition domain
QA repeat
5'
1
528
3'
1 2 3 4 5 6 7 8
NLS
NMTS
VWRPY
92 95 99
R L R P P H D N
RUNX2_ 2.1
gcc aac gcc ggc ggg gtg ctccac
---- cgg ttg cgg ccg ccc cac gac aac----
---- gcc aac gcc ggc ggg gtg ctg ttg ---
332 335 338
I T D V P R R
RUNX2_6.1
ag tgg cta cac gga tcc gcgccac
---- gcc atc acc gat gtg cct agg cgc ----
---- cgg tag tgg cta cac gga tcc gcg ----
cgg tag tgg cta cac gga tcccac
RUNX2_6.2

B

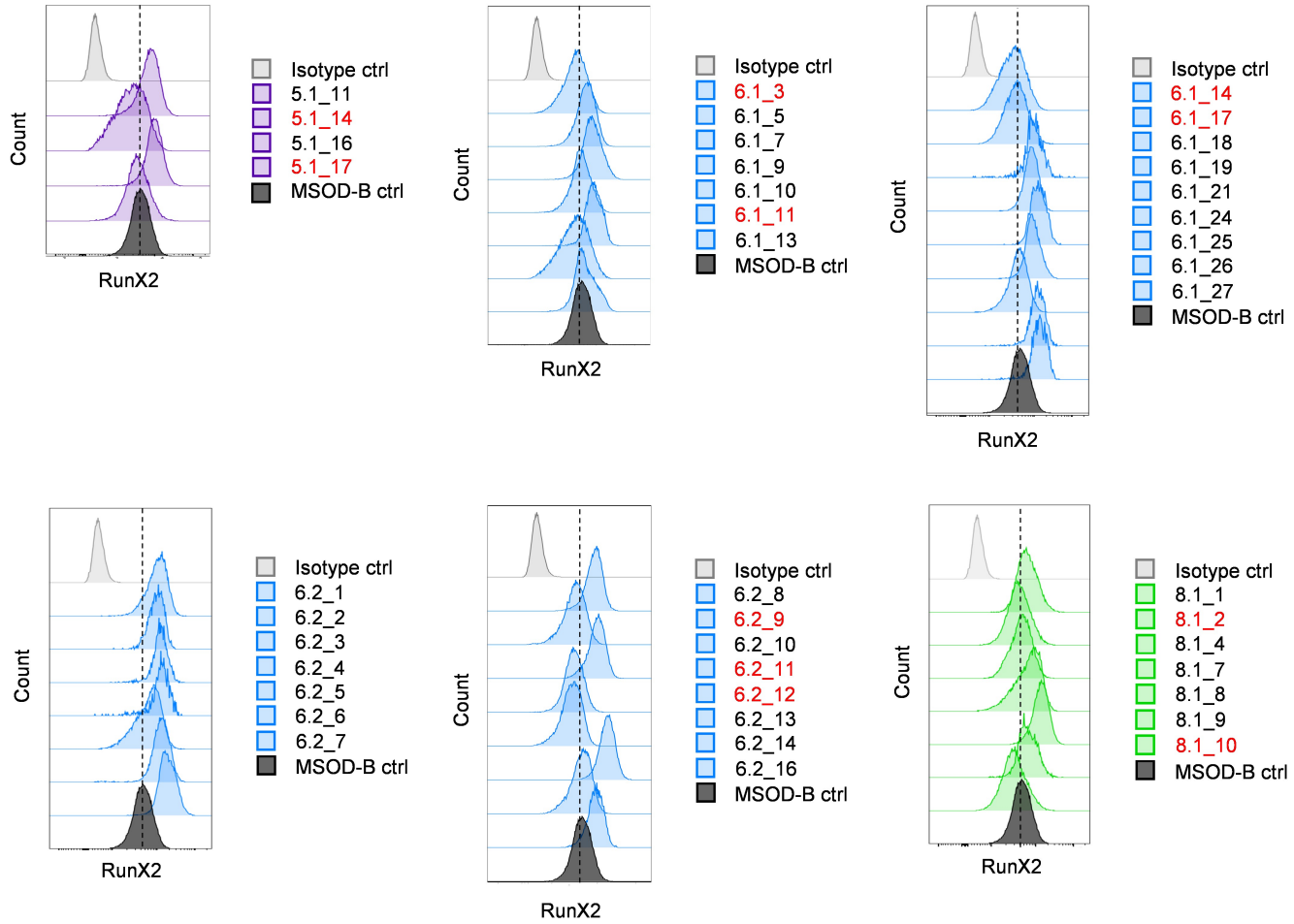
Count
RunX2
Isotype ctrl
5.1_11
5.1_14
5.1_16
5.1_17
MSOD-B ctrl
Isotype ctrl
6.1_3
6.1_5
6.1_7
6.1_9
6.1_10
6.1_11
6.1_13
MSOD-B ctrl
Isotype ctrl
6.1_14
6.1_17
6.1_18
6.1_19
6.1_21
6.1_24
6.1_25
6.1_26
6.1_27
MSOD-B ctrl
Isotype ctrl
6.2_1
6.2_2
6.2_3
6.2_4
6.2_5
6.2_6
6.2_7
MSOD-B ctrl
Isotype ctrl
6.2_8
6.2_9
6.2_10
6.2_11
6.2_12
6.2_13
6.2_14
6.2_16
MSOD-B ctrl
Isotype ctrl
8.1_1
8.1_2
8.1_4
8.1_7
8.1_8
8.1_9
8.1_10
MSOD-B ctrl

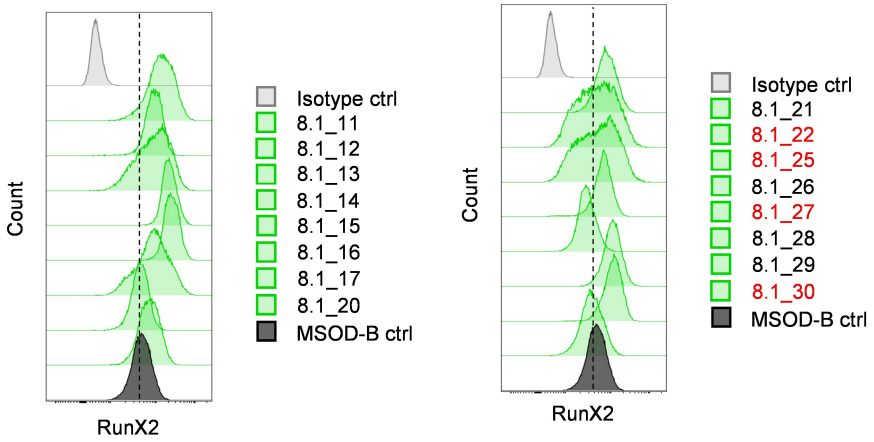
Count
RunX2
Isotype ctrl
8.1_11
8.1_12
8.1_13
8.1_14
8.1_15
8.1_16
8.1_17
8.1_20
MSOD-B ctrl
Count
RunX2
Isotype ctrl
8.1_21
8.1_22
8.1_25
8.1_26
8.1_27
8.1_28
8.1_29
8.1_30
MSOD-B ctrl

C

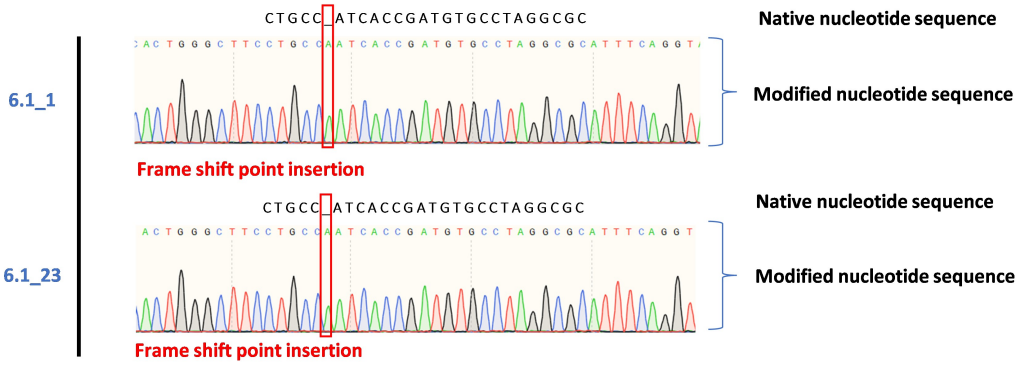
CTGCC ATCACCGATGTGCCTAGGCGC
Native nucleotide sequence
6.1_1
Modified nucleotide sequence
Frame shift point insertion
CTGCC ATCACCGATGTGCCTAGGCGC
Native nucleotide sequence
6.1_23
Modified nucleotide sequence
Frame shift point insertion

D

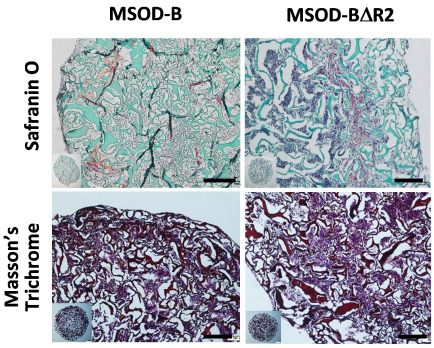
MSOD-B
MSOD-BΔR2
Safranin O
Masson's Trichrome

E

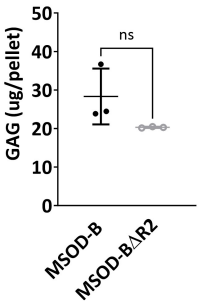
GAG (ug/pellet)
50
40
30
20
10
0
ns
MSOD-B
MSOD-BΔR2

F

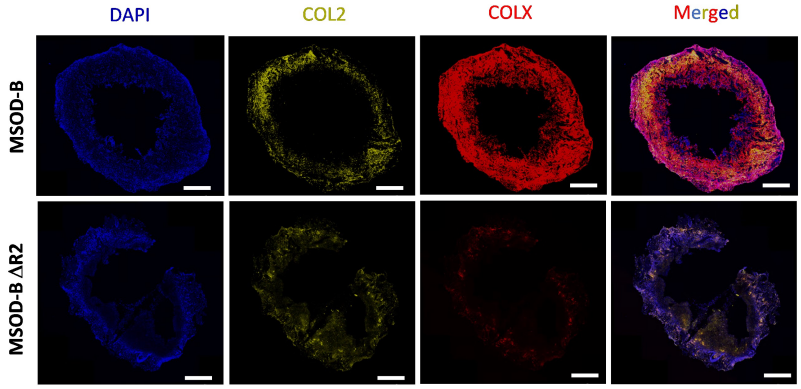
DAPI
COL2
COLX
Merged
MSOD-B
MSOD-B ΔR2

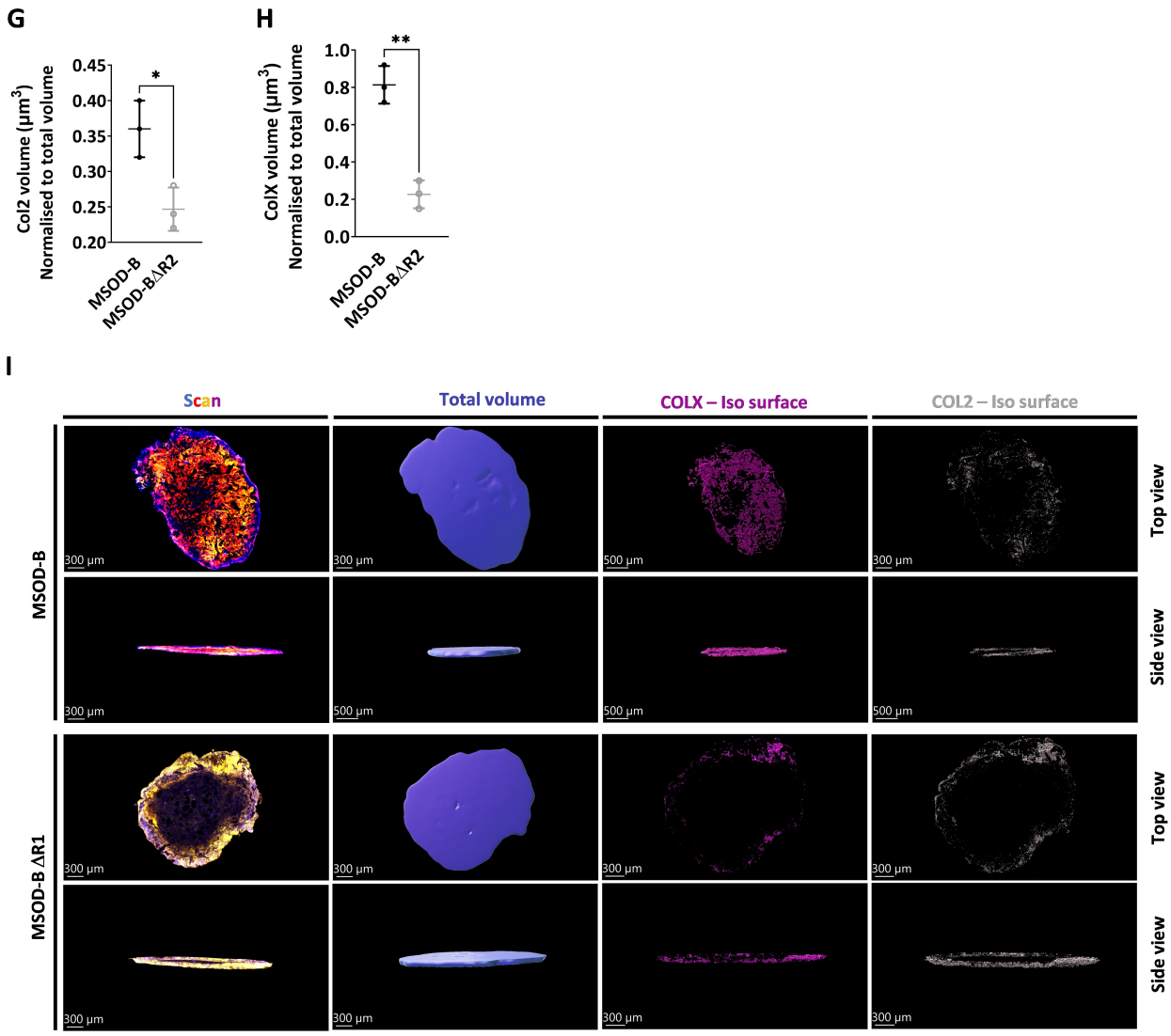

Supplementary figure 3: **RUNX2 knockout does not prevent chondrogenic differentiation but impairs hypertrophy** A) Overview of human RUNX2 exon structure, nucleotide sequences of targeting gRNAs and its corresponding amino acid sequence. B) Intracellular flow cytometry for RUNX2 detection in MSOD-B and RUNX2-edited clones. Clones whose peaks fell left of the dotted line were selected for sequencing. C) Sanger sequencing results of DNA extracted from MSOD-BΔR samples and the modifications compared to MSOD-B DNA sequence. D) Histological analysis of in vitro constructs from using Safranin O and Masson trichrome staining displayed the presence of glycosaminoglycans (GAG) and collagen content respectively, indicating the presence of cartilage formation in MSOD-BΔR2 (Scale bars = 200 µm). E) Quantitative assessment of the total GAG content (unpaired t-test, n=3, n.s. = not significant) confirms the presence of cartilage formation in both constructs thus confirming RUNX2 knockout in hMSCs (MSOD-BΔR2) retain cartilage formation. (unpaired t-test, n=3, n.s. = not significant). F) Reduction of RUNX2 expression in cartilage tissues lead to reduced hypertrophy. Representative immunofluorescence staining images of COL2, COLX and DAPI tissue section of in vitro cartilage constructs shows reduction of COLX expression in knockout construct (MSOD-BΔR2) indicating reduction of hypertrophy. (Scale bars = 500 µm). G) Quantitative analysis of the immunofluorescent staining sections using IMARIS software displayed significant difference in the expression of COL2, demonstrating reduction of cartilage formation in knockout constructs (MSOD-BΔR2) (unpaired t-test, n=3, *$p < 0.05$). H) Quantitative analysis of the immunofluorescent staining sections using IMARIS software displayed significant reduction in expression of COLX, confirming the disruption of hypertrophy in knockout constructs (unpaired t-test, n=3, n.s. = not significant). I) Representative isosurface images of immunofluorescent staining sections constructed using IMARIS software.

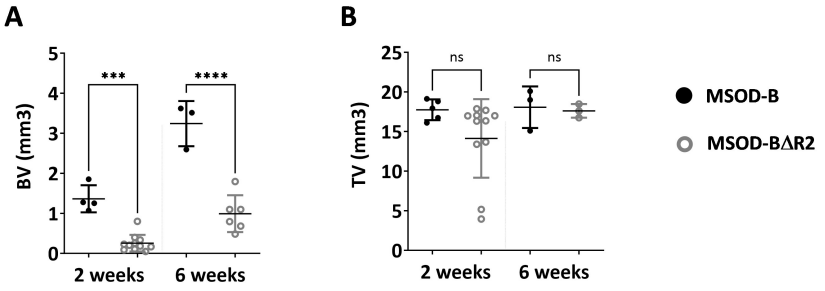

Supplementary figure 4. **RUNX2 knockout in cartilage tissues disrupts effective bone formation** A) Microtomography analysis (Bone/mineralized volume) showed very high significant difference between in vivo constructs at both two weeks and six weeks time points (One was ANOVA, n=3, *p < 0.05, ***p < 0.001). B) Microtomography analysis (total volume) showed significant difference between in vivo constructs at two weeks time point but no significant difference at six weeks time point (One was ANOVA, n=3, n.s. = not significant) (BV: Bone Volume, TV: Total Volume).

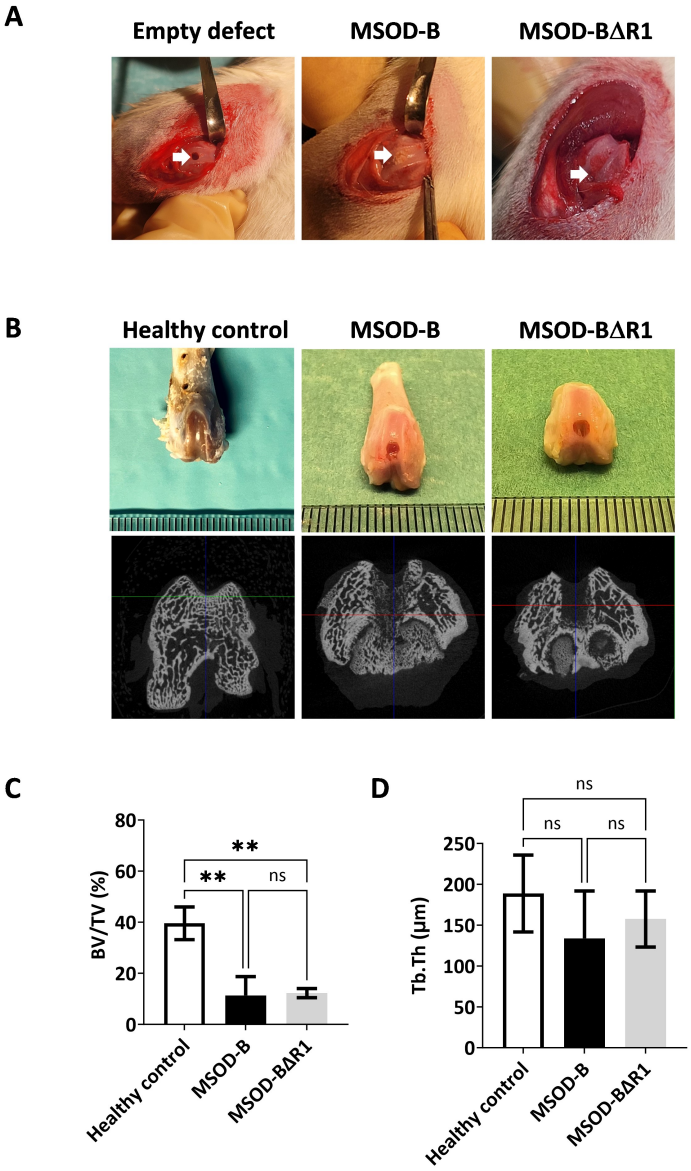

Supplementary figure 5. RUNX2 knockout in cartilage tissues exhibit better cartilage regeneration and maintenance in osteochondral defect in rats A) Macroscopic images osteochondral defect model in rats depicting in of empty defect, defect filled with MSOD-B and defect filled with MSOD-BΔR1 respectively . B) Macroscopic images of extracted rat knees depicting healthy control without any defect, defect filled with MSOD-B and defect filled with MSOD-BΔR1 respectively and microtomography images of same respective constructs. C) Microtomography-based quantification of the sample's bone/mineralized volume over their total volume (ratio). (BV: Bone Volume, TV: Total Volume). No significant difference in BV/TV is observed between MSOD-B & MSOD-BΔR1 samples despite significantly reduced BV/TV ratio in both samples compared to healthy control. One way ANOVA test, n=3 biological replicates, **$p < 0.01$. D) Image J based quantification of Trabecular thickness (tb.Th) . One way ANOVA test, n=3 biological replicates, n.s = not significant.

Supplementary table 1: Histological grading system The histological graded system is modified and adapted from previously established model as mentioned in materials and methods section. This modified scale incorporates six distinct parameters to comprehensively evaluate the quality of tissue repair

Category	Point
Cell morphology	
Hyaline cartilage	4
Mostly hyaline cartilage or fibrocartilage	3
Mostly fibrocartilage	2
Mostly non-cartilage	1
Non-cartilage	0
Matrix-staining (metachromasia)	
Normal	3
Slightly reduced	2
Markedly reduced	1
No metachromatic staining	0
Surface regularity[a]	
Smooth	3
Moderate	2
Irregular	1
Severely irregular	0
Thickness of cartilage (%)[b]	
121–150	1
81–120	2
51–80	1
0–50	0
Regenerated subchondral bone	
Good	2
Moderate	1
Poor	0
Integration with adjacent cartilage	
Both edges integrated	2
One edge integrated	1
Neither edge integrated	0
Total maximum	16

- [a] Total smooth area of the reparative cartilage compared with the entire area of the cartilage defect.
- [b] Average thickness of the reparative cartilage compared with that of the surrounding cartilage.